8-2014

NOVEL OPTICAL MICRORESONATORS FOR SENSING APPLICATIONS

Hanzheng Wang
Clemson University, hanzhew@clemson.edu

NOVEL OPTICAL MICRORESONATORS FOR SENSING APPLICATIONS

A Dissertation
Presented to
the Graduate School of
Clemson University

In Partial Fulfillment
of the Requirements for the Degree
Doctor of Philosophy
Electrical Engineering

---

by
Hanzheng Wang
August 2014

Accepted by:
Hai Xiao, Committee Chair
Eric Johnson
Lin Zhu
Zhi Gao

ABSTRACT

Optical microresonators have been proven as an effective means for sensing applications. The high quality (Q) optical whispering gallery modes (WGMs) circulating around the rotationally symmetric structures can interact with the local environment through the evanescent field. The high sensitivity in detection was achieved by the long photon lifetime of the high-Q resonator (thus the long light-environment interaction path). The environmental variation near the resonator surface leads to the effective refractive index change and thus a shift at the resonance wavelength.

In this dissertation, we present our recent research on the development of new optical microresonators for sensing applications. Different structures and materials are used to develop optical resonator for broad sensing applications. Specifically, a new coupling method is designed and demonstrated for efficient excitation of microsphere resonators. The new coupler is made by fusion splicing an optical fiber with a capillary tube and consequently etching the capillary wall to a thickness of a few microns. Light is coupled through the peripheral contact between inserted microsphere and the etched capillary wall. Operating in the reflection mode and providing a robust mechanical support to the microresonator, the integrated structure has been experimentally proven as a convenient probe for sensing applications. Microspheres made of different materials (e.g., PMMA, porous glass, hollow core porous, and glass solid borosilicate glass) were successfully demonstrated for different sensing purposes, including temperature, chemical vapor concentration, and glucose concentration in aqueous solutions. In

addition, the alignment free, integrated microresonator structure may also find other applications such as optical filters and microcavity lasers.

DEDICATION

I dedicate my dissertation work to my family and friends. A special feeling of gratitude to my wife Xinxin Zhang has never left my side and is very special. My loving parents, Faqing Wang and Cuiying Shi whose words of encouragement and push for tenacity ring in my ears.

I also dedicate this dissertation to my other family members and many friends who have supported me throughout the process. I will always appreciate all they have done.

I dedicate this work and give special thanks to my son Tony Xijia Wang, who brought me tremendous joy and courage during my research and life.

ACKNOWLEDGMENTS

I wish to thank my committee members who were more than generous with their expertise and precious time. A special thanks to Dr. Hai Xiao, my committee chairman for his countless hours of reflecting, reading, encouraging, and most of all patience throughout the entire process. I would like to thank Dr. Eric Johnson, Dr. Lin Zhu, and Dr. Zhi Gao for agreeing to serve on my committee.

I would like to acknowledge and thank my school division for allowing me to conduct my research and providing any assistance requested. Special thanks go to the members of Electrical Engineering Department for their continued support.

I also want to give my special thanks to Dr. Richard K. Brow and Dr. Cheol-Woon Kim, for the supply of various types of glass microspheres.

Finally, I would like to thank my lab mates, Xinwei, Lei Yuan, and others who assisted me with this project. Their cooperation and made the completion of this research an enjoyable experience.

TABLE OF CONTENTS

Page

Table of Contents (Continued)

Page

Table of Contents (Continued)

Page

LIST OF TABLES

Table Page

LIST OF FIGURES

List of Figures (Continued)

Figure Page

List of Figures (Continued)

Figure Page

List of Figures (Continued)

Figure Page

List of Figures (Continued)

Figure Page

List of Figures (Continued)

Figure Page

LIST OF ACRONYMS

CQEM – Cavity Quantum Electrodynamics

EMI – Electromagnetic Interference

FBG – Fiber Bragg Grating

FFSCT – Flexible Fused Silica Capillary Tube

FWHM – Full Width at Half Maximum

FSR – Free Spectrum Range

ILCMRR – Ionic Liquid Core Microring Resonator

PGM – Porous Glass Microsphere

PMMA – Poly (methyl methacrylate)

PWHGM – Porous Wall Hollow Glass Microsphere

RI – Refractive Index

SEM – Scanning Electron Microscope

SPR – Surface Plasmon Resonance

SS – Stainless Steel

TE – Transverse Electric

TM – Transverse Magnetic

WGM – Whispering Gallery Mode

CHAPTER ONE

INTRODUCTION

1.1 Optical Microresonator: Concept and Fabrications

Optical microresonator has been investigated for a few decades for its broad applications in optical filter, quantum electrodynamics, lasers and sensors. Spherical, circular, ring, toroid and rectangular shaped microcavities have attracted great interest as optical microresonators [1-4]. These axially symmetric structures trap light in a small volume in the form of whispering-gallery modes (WGMs), resulting in optical resonances in the transmission spectrum. The concept of WGMs in optical microresonator is defined as circular electromagnetic waves supported by transmission from boundaries of the symmetrical structure. By using highly transparent, low scattering loss material, such as silica, the WGMs can provide extremely high values of Q-factor in a small mode volume. The Q is mainly limited by the material attenuation and scattering loss contributed by surface roughness and geometrical imperfections. The high index difference at the boundary and relatively larger curvature (typically exceeds several wavelengths) guarantee the minimization of radiative loss and bending loss.

There are different approaches to fabrication dielectric microresonators. Microsphere can be fabricated by fusion splicing an optical fiber or fiber taper, or by using laser irradiation and focusing on the fiber or taper ends [5]. Microdisk or microtoroid can be made by photolithography and chemical etching [6]. Microfluidic ring resonator is made by an etched cylindrical tube integrated with chemical fluid [4, 7, 8]. The slot-waveguide ring resonator can be fabricated by using a dual surface-energy

adhesive film to bond a hard plastic shell [9] or using SU-8 epoxy negative photoresist [10].

According to different purposes, various materials and fabrication approaches are used. A dye-doped microsphere significantly enhances the lasing efficiency, which also contributes to an enhancement in the observed Q-factor [11, 12]. Optical microfiber knot resonators were demonstrated with air and MgF_2 substrate with Q at 50,000 [13]. Optical resonance can be well maintained when immersed into water or a low-index substrate with potential optical signal processing, sensing applications.

1.2 Applications of Optical Microresonator: Optical Filter, Cavity QED and Laser

One of the applications based on optical microresonator is optical filter. Sophisticated control of the devices wavelength response can be possibly achieved by combing optical microresonators appropriately.

Little et. al. has analytically shown a compact, narrow band, and large free spectral range optical channel dropping filter, using optical microring resonators side coupled to signal waveguides [14-16]. The performance between multiple coupled rings and a single resonator were presented that the filter performance can be improved providing larger out-of-band signal rejection, and a flat pass band, shown as the following figures.

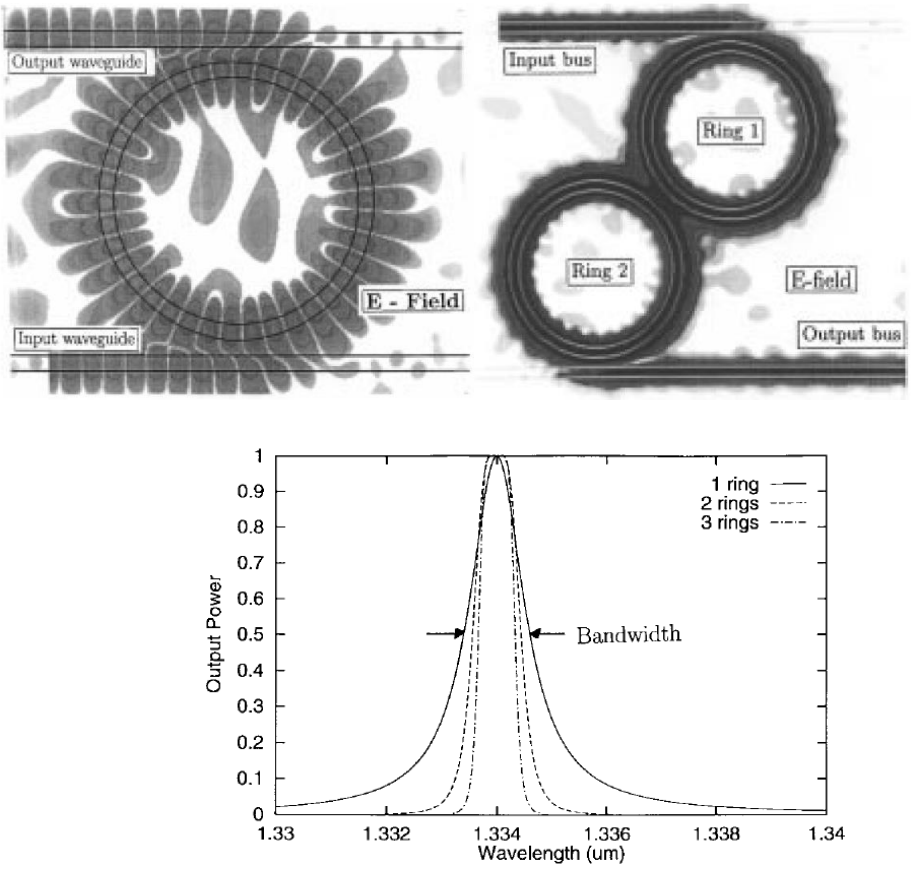

Fig. 1.1. Instantaneous electric field amplitude in the ring filter near the resonant wavelength λ_o = 1.334 μm for single and double ring resonators. Bottom: a comparison of the pass band characteristics of filters composed of one, two, and three coupled rings [15].

With the demonstration of 1 to 11 coupled cavities, a device of high-order microring resonators can be obtained. These filters present low loss, flat tops, and out-of-band rejection ratios with more than 80 dB [17]. Potential commercial applications can be achieved with these performances. Example of a 6^{th} order filter is shown as following:

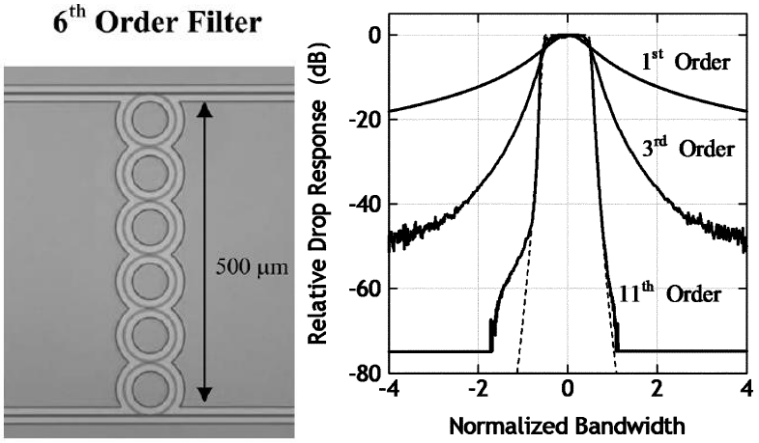

Fig. 1.2. Example of a sixth-order microring resonator filter and measured response for first-, third-, and 11th-order microring resonator [17].

Recently, an electrically reconfigurable silicon microring resonator-based filter with waveguide-coupled feedback was demonstrated [18]. In this design, a nearly uniform resonance line shapes over multiple free-spectral ranges by nearly phase matching the feedback and the microring, shown as the following figure.

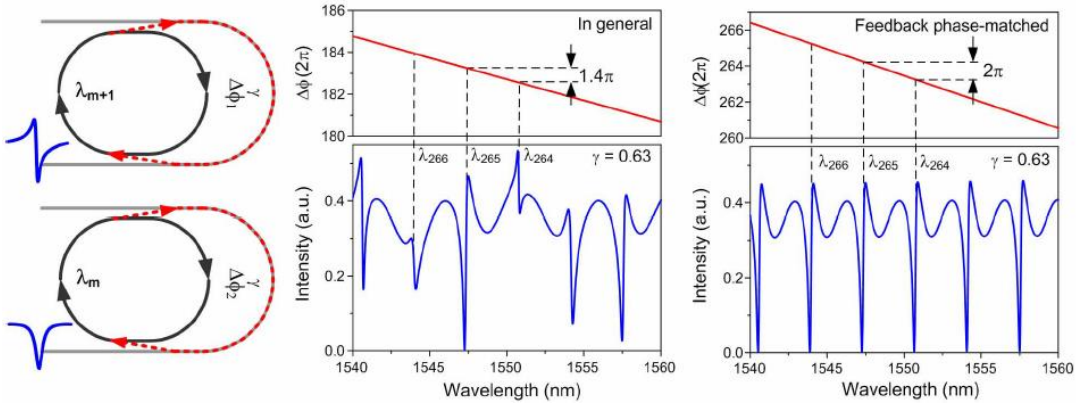

Fig. 1.3. Illustration of the resonance-dependent line shapes in general cases [18].

The feedback phase and amplitude are tuned through the free-carrier plasma dispersion and absorption effect by forward biasing a laterally embedded p-i-n diode, and the transmission resonances depends on the attenuated feedback coupling [18].

WGM microcavities have been investigated for cavity quantum electrodynamics (CQED) experiments for many years. The combination of the low cavity losses, relative ease of fabrication and small mode volumes makes them promising candidates for experiments in CQED [19]. Microtoroidal shaped silica cavity supported by a silicon pillar allows an extra level of geometric control and strong coupling compared to spherical cavity [20]. This not only retains the high-Q factors of spherical cavity, but also shows significant advantages in control, mode structure and fabrication reproducibility.

The properties of the microtoroidal optical resonator are demonstrated in [20]. The mode volumes of silica toroidal microresonator are given by the equation [20]:

$$V_m = \frac{\int_{V_Q}^{V_Q} \epsilon(\vec{r}) \left|\vec{\mathrm{E}}(\vec{r})\right|^2 d^3\vec{r}}{\left|\vec{\mathrm{E}}_{max}\right|^2} \qquad (1.1)$$

Where V_Q represents a quantization volume of the electromagnetic field and $\left|\vec{\mathrm{E}}\right|$ is the electric field strength [21].

Spillane et. al. [22] introduced a technique to both measure ideality of a range of coupling strengths and provide a diagnostic of parasitic coupling within the fiber taper waveguide junction. Meanwhile, Louyer et. al. demonstrated a tunable WGM resonator using bottle shaped cylinder [23]. The modes spacing for this resonator was shown as one order of magnitude smaller than an equatorial WGM. This design is suited to be combined with a surface trap for cold atoms trapping into the resonator mode.

Microcavity lasers based on optical microresonator platform have also been investigated. The small mode volume and low threshold make it an ideal micro laser device. A thin semiconductor Microdisk with optical confinement within the disk plane provides an optical microresonator with single-mode, ultralow threshold lasers [24]. Optically pumped InGaAs quantum well provides sufficient gain at 1.3 and 1.5 μm wavelengths with low threshold pump power at 100 μw.

Raman laser using spherical optical resonator with ultralow-threshold were demonstrated [25]. A series of Raman oscillation peaks located around 1670 nm can be observed at the pump of 1550 nm. In the following figure, the spectrum of a 70 μm diameter microsphere laser with pump laser power of 2 mW is presented.

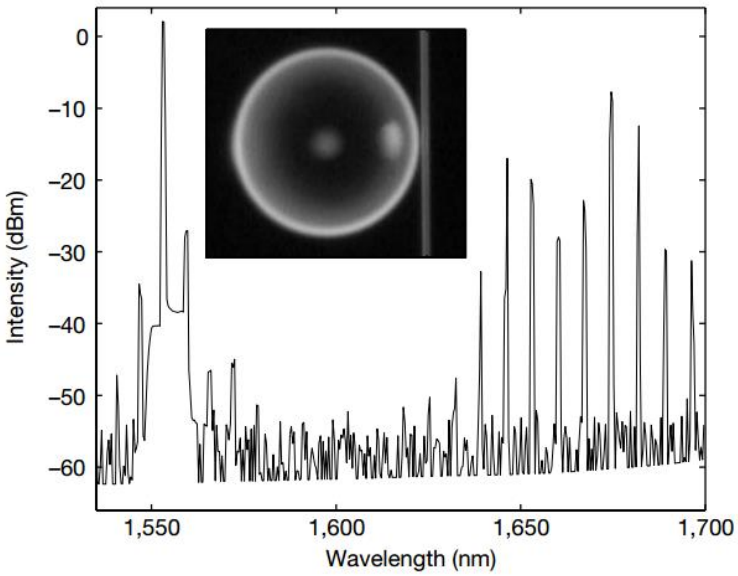

Fig. 1.4. Raman oscillations using a microsphere coupled to a fiber taper [25].

The efficiency of the Raman oscillator was investigated [25]. The threshold was obtained by decreasing the pump power until a single emission wavelength was observed.

The measured threshold is 86 μW, which is 1,000 times lower than that of using microdroplets [26].

Rare earth doped optical resonator microlaser on a silicon chip with solgel process was demonstrated [27, 28]. High Q-factor obtained by toroidal microcavity with continuous lasing with threshold of 660 nW was obtained [28].

The microsphere resonator with thin film gain layer shows an important effect on laser dynamics [27]. Optical coupling to the spherical cavity using optical fiber taper serves for both pumping and laser extraction. The following figure shows the up conversion photoluminance at different coupling zones.

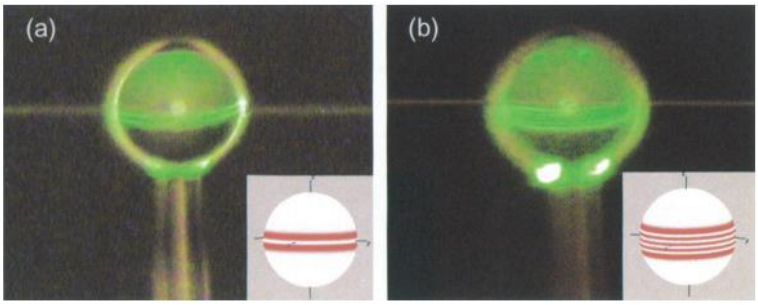

Fig. 1.5. Images of the WGMs in the taper-sphere coupling zone: (a) l - m = 1, (b) l – m = 4 [7].

Other microlaser related topics including microresonator based optical frequency combs [29, 30], parametric frequency doubling [31], optical hyperparametric oscillation [32], and phase-matched second-harmonic generation [33] have been attracted great interest for microresonator laser applications.

1.3 Optical Microresonator for Sensing Applications

Optical sensing [34-36] technique has been developed for the last a few decades and finds broad applications in structure monitoring [37-41], food industry [42, 43], chemical detection [44-49], temperature measurement [50-53] and bio-sensing [54-57], etc. There has been intense research and development interest in fiber grating sensors over the past decades [34, 58-60], and fiber sensors provide advantages such as electrically passive operation, electromagnetic interference (EMI) immunity, high sensitivity, and multiplexing capabilities [34, 60]. Various types of gratings are investigated, including uniform fiber Bragg gratings (FBG) [60], chirped gratings [61-63], tilted FBG [64, 65], long period-based grating sensors [50, 59, 66, 67], and interferometric sensor systems based on grating reflectors [58].

Surface Plasmon Resonance (SPR) phenomenon has also been used for sensing more than three decades and this method made great strides in sensing applications [68-70]. Commercialized SPR becomes a central tool for characterizing and quantifying biomolecular interactions [71-73]. However, the detection limit of SPR biosensor is an issue compared to other optical sensors [72, 74].

Additionally, optical interferometers have also been studied for broad sensing applications. Michelson interferometer, Mach-Zender interferometer, Fabry-Perot interferometer and multimode interferometer have shown advantages in high sensitivity, fabrication ease, low cost and fiber component compatibility [34, 36, 75]. These double interference devices usually require large sampling areas (analyte volumes) [76].

WGM optical microresonators sensors [77-81] have shown its advantages in detection limit, miniature size and high sensitivity when combined with specific material or structures [77-81]. Optical resonator finds its broad applications in chemical sensing, thermal sensing, pressure sensing, biological sensing, etc [2, 6, 77-82].

When pure fused silica microsphere is used, the optical resonator exhibits a high Q [1]. The spectra position of the resonance shifts in response to the refractive index change in surrounding medium [83]. The strong interaction between the light and surrounding due to the extremely high Q yields a sensitivity of approximately 30 nm/RIU (refractive index units). When a high spectral resolution sensor system is employed (0.01 pm), the detection limit of refractive index change can achieve 10^{-7} RIU [83]. Coiled microfiber resonator together with low loss Teflon coating can highly improve the sensing performance [84, 85]. Due to its high-Q and enhanced adsorption, the sensitivity can be as high as 700 nm/RIU and a refractive index resolution of 10^{-10} can be predicted [84]. The setup is shown as following:

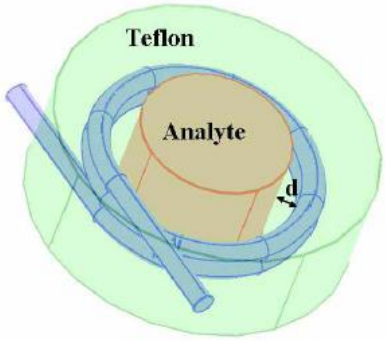

Fig. 1.6. Schematic of the coated all-coupling nanowire microcoil resonator [84].

The sensitivity of this nanowire coil resonator device has been studied in two typical configurations and its dependence on the morphology, such as nanowire diameter and coating thickness [85].

On-chip integrated optical resonator sensors are also demonstrated miniature size and inexpensive cost [76]. Though the Q (5×10^3) is relatively low due to the material and coupling scheme, the whole setup turns out to be convenient for sensing purpose. A measurement of refractive index change of 10^{-4} is demonstrated experimentally [76].

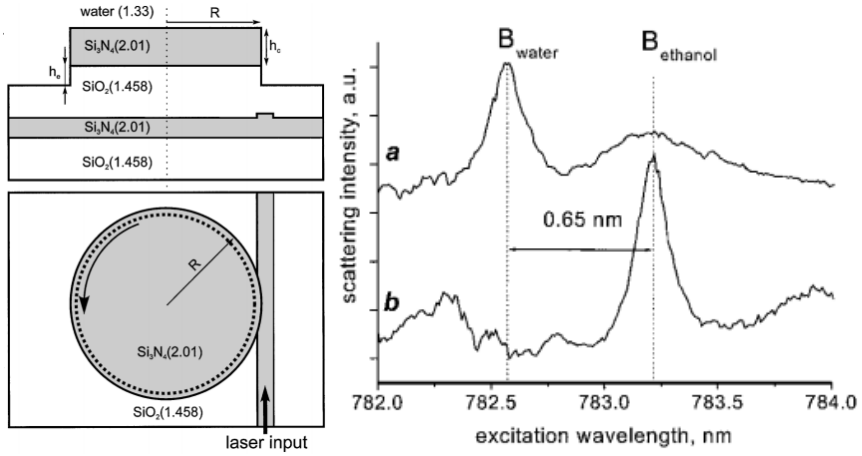

Fig. 1.7. Cross section and view of an integrated optical sensor and its RI sensing response [76].

On-chip sensor based on polymer ring resonator was demonstrated for RI sensing with a higher Q (20,000). This device was fabricated by direct imprinting technique with thermal re-flow treatment [86]. The resolution can achieve 10^{-7} RIU and a detection limit of 250 pg/mm^2 of molecule coverage on the ring surface. This shows the potential of the optical resonator for label-free sensing and the combination with microfluid channels for drug discovery, environmental monitoring and chemical analysis [86].

In chemical and bio-sensing applications, the high Q of the optical microresonator offers the potential of high detection limit and sensitivity [77, 78, 87-89]. The equivalently long interaction between the resonance and surrounding media can provide a sufficient phase shift for sensing and measurements [87]. The microsphere WGMs resonator has been demonstrated to respond to monolayer of protein adsorption [90]. Microdisk [91] or microtoroid [6, 92] resonators have been shown with sensitivity enhancement and analyte reduction in comparison with waveguide sensors. In addition, clusters of polystyrene microspheres (10 μm) were used for optical in situ biosensing with each cluster exhibits a specific WGM spectrum that can be considered as its fingerprint and identification of traced clusters [93]. Nanoparticle detection using microtoroid resonator [6] and single atom detection [94] were also investigated based on WGMs resonator platform.

1.4 Motivation of This Dissertation

Optical microresonator with high-Q, miniature size and high detection sensitivity make it a good candidate for sensing applications, such as chemical detection, thermal sensing, refractive index measurement, etc. It is envisioned that these optical microresonator based sensors may find broad important applications in various areas of biochemical analysis, drug discovery, disease diagnostics, food industry, and environmental monitoring. However, traditional optical resonator sensors require stable lab-based environment and its sensitivity needs improvement. Our approaches include the change to porous structure and sensitive material of the microspheres and an

enhancement of coupling robustness. The goal of this research is to conduct research on the development of device, material and system for the target of the improvement of sensor sensitivity as well as environment tolerances. The specific research steps and objectives include:

1. High sensitivity chemical detection: porous glass hollow core microsphere was used to integrate with fiber taper. Transmission resonance spectra was monitored and demonstrated with wavelength shift according to the surrounding media change. Various types of chemical vapor were tested and selectivity can be observed at same vapor concentration level. An increasing of detection sensitivity of 30 – 100 times was noticed compared to that of a solid glass microsphere resonator.

2. Microring resonator with ionic liquid core was tested for CO_2 absorption. The sensitivity was enhanced due to the high absorption rate of ionic liquid. This novel device can be potentially used in environmental monitoring and control applications.

3. A novel fiber pigtailed thin wall capillary coupler was designed and demonstrated for its capability of coupling microsphere optical resonator. The cylindrical wall coupler overcame the fragility nature of the fiber taper coupling. The reflection based coupling and resonance signal realized a convenient resonator sensor probe for practical use in field test.

4. The thin wall capillary-coupled optical resonator was tested for different sensing purposes. In order to enhance the sensitivity, specific material or structures were applied. For the purpose of ethanol vapor detection, a porous glass sphere was used as an optical resonator and fully extended its molecule adsorption capability for the

enhancement of the sensitivity. In thermal sensing, a polymer sphere was tested with higher thermal response to silica bead. In refractive index sensing, the capillary cavity was sealed and dipped into the glucose sample for resonance intensity measurement as a function of glucose concentration change. The sensing probe was proven as an effective and convenient tool for in-situ sensing applications.

5. The performance of the optical resonator sensors was proved with the test of their sensitivity, repeatability and reliability.

1.5 Dissertation Outline

Chapter 2 discusses the porous wall hollow glass microsphere (PWHGM) and its use as an optical resonator for chemical vapor detection. An introduction of PWHGM will be given in this chapter as well as its original use as a protein carrier. Coupling principle and experimental tests will be demonstrated in different chemical vapor responses: deionized water vapor, nitrogen gas, ethanol vapor and acetone vapor. A sensitivity comparison between solid microsphere and PWHGM will be given.

Chapter 3 presents an analytical study on the sensitivity differences as a function of structure and material variations. The computational model on the PWHGM optical microresonator will be shown with different parameters: wall thicknesses, radius and modes selection. Comparison between the analytical study and experimental results will be shown thereafter.

Chapter 4 demonstrates the new fiber pigtailed thin wall coupler and its integration with optical microresonator. The fabrication steps and coupling principle will

be discussed. The advantages of the coupler will be discussed and a reflection resonance spectrum will be demonstrated.

Chapter 5 discusses the applications of the thin wall capillary coupled resonator for sensing purposes. Chemical vapor detection, thermal sensing and refractive index measurement will be demonstrated. The experimental results will present its efficiency as a resonator sensor probe in practical tests.

Chapter 6 shows a new ionic liquid core microring resonator and its use as a CO_2 detector. The coupling scheme and sensing result will be presented. Experimental results will show the sensitivity of the resonator and its time response of CO_2 absorption.

Chapter 7 summarizes the work and proposes the scope for future research.

Appendix A offers a details explanation of the fiber taper fabrication steps as well as the fixation of the PWHGM onto a fiber end.

Appendix B investigates the fiber pigtailed thin wall coupler manufacture and its integration with microsphere.

CHAPTER TWO

POROUS GLASS MICROSPHERE OPTICAL MICRORESONATOR

2.1 Porous Wall Hollow Glass Microsphere

In chemical detection, microspheres have also been coated with a compound to minimize the influence of the external environment and to improve the performance of the sensor [1, 95-98]. Porous structures have been proposed for chemical sensing [96-98]. Seo reported a method for enantioselective separation and catalysis using an organic porous material [96]. Danil showed a microporous manganese formate that exhibits permanent porosity, high thermal stability, and highly selective gas sorption properties [97]. Based on the adsorptive nature of porous structure, microspheres coated with porous zeolite were proposed to enhance molecule adsorption for chemical sensing [98]. However, it has been observed that controlling the coating quality can be difficult.

In this chapter, an optical microresonator based on a porous-wall hollow glass microsphere (PWHGM) is reported for chemical vapor detection. Due to the porous wall and hollow core of the PWHGM, chemical vapor molecules can freely pass in and out of the pores and change the effective refractive index of the microsphere, which in turn induces a shift in the resonant wavelength of the resonator. Concentration change of chemical vapor can then be measured by monitoring the wavelength shift.

PWHGMs are composed of a chemically stable sodium borosilicate glass material constructed in the form of a hollow central cavity surrounded by a shell penetrated with tortuous network of nanometer-scale channels [99]. The PWHGMs employed in this study were provided by the MO-SCI Corporation. The glass is heat treated to form a

distinct silica-rich and sodium borate phase with an interconnected morphology. When the glass is drawn by a leaching process, it produces interconnected pores or channels. The diameter of the PWHGMs ranges from 10 to 100 μm. Generally, the pore sizes range from 20 to 200 nm and the shell thickness is between 0.5 to 2 μm. The shell thicknesses and porous apertures are proportional to the size of the spheres and the pore size can be tuned by the bead formation process. Fig. 2.1 shows scanning electron microscope (SEM) images of a PWHGM. The small hole shown in Fig. 2.1 (a) at the four o'clock location on the sphere is intentionally created by gently pressing the PWHGM with a glass slide so that the detailed structure of the shell shown in Fig. 2.1 (b) can be observed. A magnified cross-sectional image of the square area is shown at the top left corner of Fig. 1(b), from which the worm-like porous structures can be clearly seen.

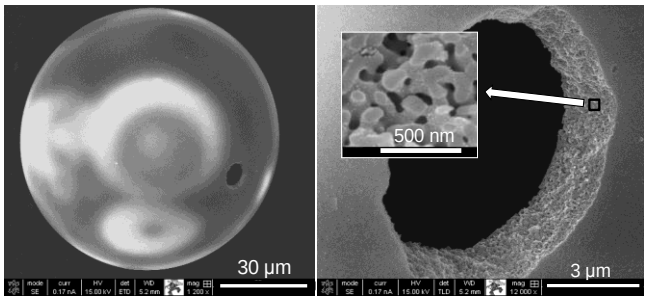

Fig. 2.1. (a) Overview of a PWHGM; (b) the hollow cavity and porous structure of the PWHGM [100].

2.2 Porous Wall Hollow Glass Microsphere Optical Resonator

2.2.1 Schematic and Experimental Setups

The experimental setup is shown in Fig. 2.2. A fiber taper with a length of ~1 cm and a center diameter of ~2 μm is fabricated from a section of single mode fiber (Corning

SMF-28) using a fiber stretching system. A PWHGM is placed in contact with the taper using a micro positioning system. When light from a tunable laser passes through the taper, part of it is coupled into the PWHGM microresonator where the whispering gallery mode is excited [1]. If the PWHGM is immersed in a chemical vapor, molecules are able to freely pass into the pores of the PWHGM. Concentration change of the vapor will alter the effective index of the resonator, shift the resonant wavelength, and be detected by measuring the wavelength shift via a photo detector.

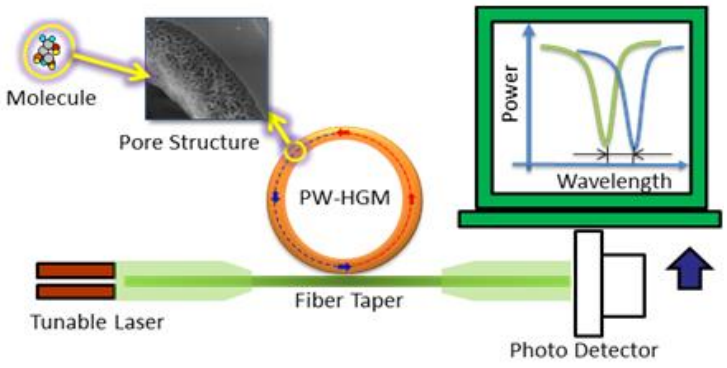

Fig. 2.2. Schematic of PWHGM micro-resonator in molecule adsorption detection [100].

2.2.2 Transmission Resonance Spectrum

Figrue. 2.3 shows a typical normalized transmission spectrum of a PWHGM resonator with a diameter of 75 μm in air. The diameter was measured using a measuring microscope. It was found that the amplitude of the resonance was proportional to the size of the sphere. For the 75 μm diameter PWHGM resonator, the Q factor was calculated to be 2.49×10^3 at the resonant wavelength of 1549.27 nm. The corresponding full width at half maximum (FWHM) was 0.62 nm and the free spectrum range (FSR) was 6.61 nm.

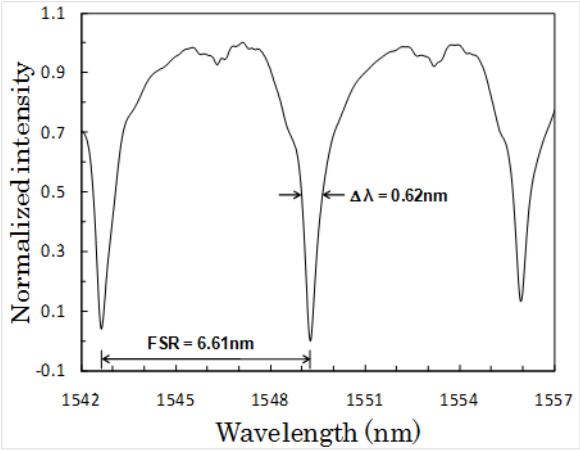

Fig. 2.3. Transmission spectrum of a PWHGM resonator in air [100].

Compared with traditional microresonators based on solid glass beads, the Q factor is about 10^3 times lower due to the higher scattering loss caused by the porous structure of a PWHGM. However, the porous structure that enables the mechanism that makes a PWHGM resonator a worthwhile chemical vapor sensor. Because molecules smaller than the pores can be easily adsorbed to the resonator and therefore detected by measuring the resulted resonant wavelength shift.

2.2.3 Porous Wall Hollow Glass Microsphere Resonator for Chemical Sensing

To demonstrate the capability of the PWHGM microresonator for use as a chemical vapor sensor, a series of experiments were performed by monitoring the response of the resonator to various types of vapors. During the experiments, the PWHGM microresonator was placed in a chemical vapor chamber, which was connected to the output of a bubbler placed inside an ice bath. The input end of the ice-immersed bubbler was linked to a nitrogen gas tank. The chemical-water solution sample was filled

in the bubbler and nitrogen gas served as a carrying gas, which under the control of a flow meter; brought the volatized chemical from the chemical sample into the test chamber. The vapor concentration was varied by changing the concentration of the solution. In all the experiments, the flow rate of the nitrogen was held constant. The resonator was interrogated by a broadband light source and the transmission spectrum was recorded by an optical spectrum analyzer.

Vapors containing different concentrations of ethanol were measured. The results are shown in Fig. 2.4, from which it can be seen that an increase in the vapor concentration results in a corresponding shift in the resonant wavelength toward longer wavelength. The inset shows the wavelength shift as a function of the solution concentration. Measurements were performed five times at each concentration with the error bars shown in the figure. The curve-fitting of the resonant peaks was performed to eliminate the random intensity noises. The standard deviations based on the five-time measurement data at 5, 10, 25, 50 and 100% concentrations were 0.03, 0.03, 0.03, 0.04, 0.04 nm, respectively.

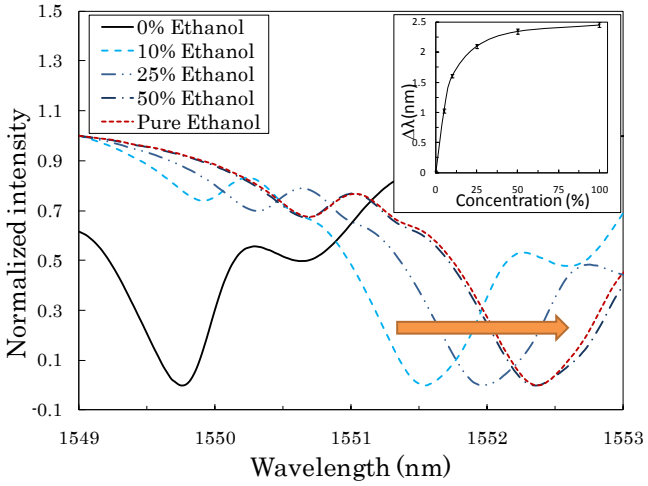

Fig. 2.4. Responses of the PWHGM sensor to vapors of different concentration of ethanol solutions. Insert: wavelength shift as a function of ethanol vapor concentrations [100].

The responses of the PWHGM microresonator sensor to different chemical vapors have also been tested. The spectrum change and resonant wavelength shift of the sensor to vapors from deionized (DI) water, pure ethanol and pure acetone, all mixed in a nitrogen carrier gas, are shown in Fig. 2.5.

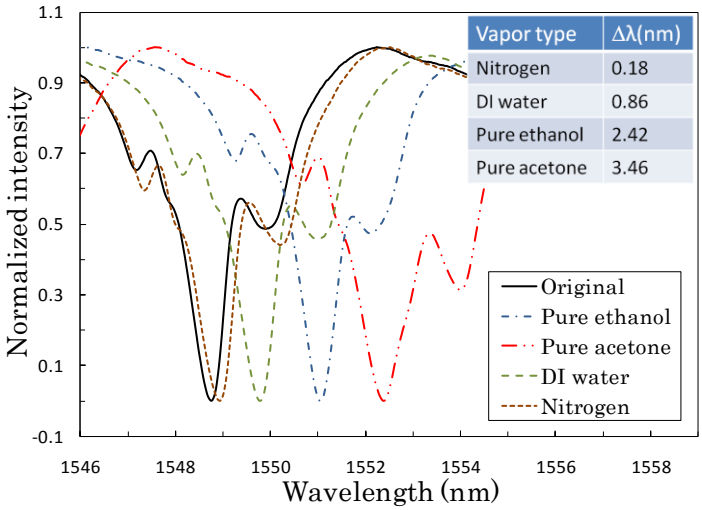

Fig. 2.5. PWHGM microresonator optical spectrum in different chemical vapor types [100].

2.2.4 Sensitivity Enhancement

In order to show the sensitivity improvement of PWHGM microresonators compared with those of traditional solid microsphere resonators, the responses to acetone and ethanol vapors from different concentration solutions were measured. Fig. 2.6 shows the wavelength shift as functions of the solution concentration for both kinds of resonators. For better visualization, the wavelength shifts of the solid microsphere were

magnified by ten times in Fig. 2.6. The resonant wavelength of the resonator increased rapidly when the vapor concentration was low. The wavelength shift became slow at high vapor concentrations. The nonlinear relationship between the wavelength shift and the concentration agree qualitatively with the Langmuir adsorption model. The response curves suggested that the PWHGM microresonator sensor has higher sensitivity at lower vapor concentrations. The PWHGM has shown different sensitivities to different types of chemical vapors. Adsorption of chemical vapors of different refractive indices may result in different amount of changes in the effective index of the glass-vapor mixture. Therefore, it is expected that the sensitivity of the PWHGM will depend on the size and polarity of the molecule, as well as the adsorption strength towards a specific molecule.

From Fig. 2.6 it can be seen that when compared with the traditional solid microsphere resonator under the same experimental conditions, the vapor detection sensitivity of the PWHGM microresonator is significantly higher. The wavelength shift of PWHGM at 100, 25 and 5% acetone-water vapor were measured to be 3.46, 2.74 and 1.69nm, respectively. In contrast, the wavelength shifts of the solid microsphere at 100, 25 and 5% acetone-water vapor were measured to be 0.15, 0.14 and 0.07nm, respectively. The sensitivity of solid microsphere is apparently lower due to the nonporous surface, which lacks the capability of adsorbing molecules.

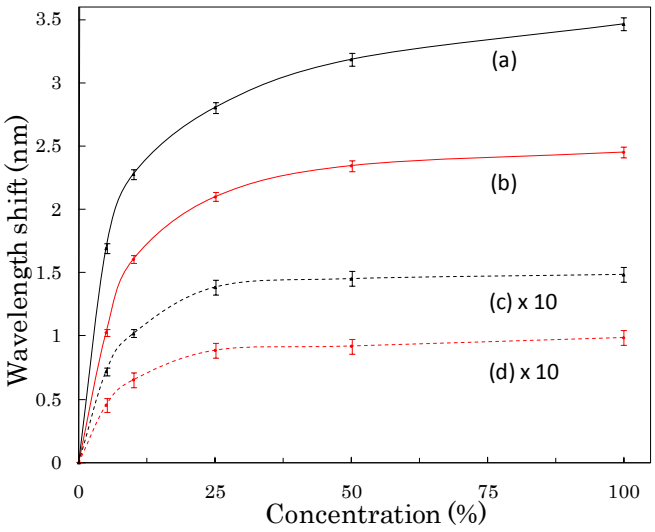

Fig. 2.6. Sensitivity comparison of PWHGM and solid microsphere for chemical vapor detection. (a) Acetone vapor on PWHGM; (b) Ethanol vapor on PWHGM; (c) Acetone vapor on solid microsphere and (d) Ethanol vapor on solid microsphere. The shifts in (c) and (d) are multiplied by ten times for better visualization [100].

In summary, a PWHGM was investigated as an optical microresonator for chemical vapor detection. Adsorption of chemical vapor molecules into the nano-sized pores in the wall of the PWHGMs changes the effective refractive index of the material, causing a shift in the resonance spectrum towards longer wavelengths. The amount of wavelength shift increased as the vapor concentration increased. It is expected that the sensitivity of the PWHGM will depend on the porosity and thus the averaged pore size. After calibration, this deterministic relation can be used for chemical vapor sensing. The Q-factor of the PWHGM is significantly smaller than that of a solid microsphere. However, because of the porous structure, it showed a higher sensitivity compared with a solid microsphere when used for chemical vapor detection.

CHAPTER THREE

SIMULATION AND MODELING OF THE POROUS GLASS MICROSPHERE OPTICAL MICRORESONATOR FOR SENSING APPLICATION

3.1 Introduction of Porous Glass Microsphere Modeling

In this chapter, the aim of our work is to theoretically explain the effect of different spherical resonator structures on chemical detection sensitivities. The computational model on the PWHGM microresonator is presented and the comparison of its corresponding experimental results was shown.

The structures and resonance spectra of the WGMs in excited microsphere resonators have been studied theoretically in recent years [1, 98, 101-103]. Generally, spherical coordinates were used to characterize the mode numbers in WGM: angular mode *l*, azimuthal mode *m* and radial mode *v*. Fig. 3.1 demonstrate the models of WGMs in the solid glass microspheres and PWHGM. The solid glass sphere model is shown in Fig. 3.1 (a) with n_0=1.0 and n_s=1.45, and the PWHGM model in Fig. 3.1 (b) shows n_s=n_0=1.0 and n_p=1.45.

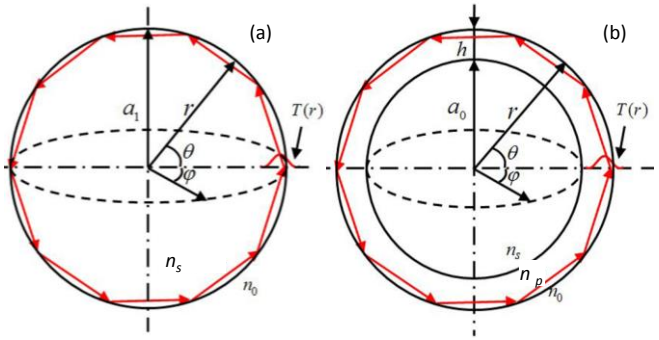

Fig. 3.1. WGM models in (a) solid glass sphere and (b) PWHGM [104].

3.2 Analytical Study and Simulation on Porous Glass Microresonator Sensor

3.2.1 Analytical Study on Porous Glass Microsphere Optical Resonator

The total internal reflection of light along the interface of microsphere wall and surroundings is shown in red arrowed lines in Fig. 3.1. The resonance wavelength λ_R can be expressed by the characteristic equation [98, 101-103]:

$$\eta_s \frac{\chi_l'(n_0 k a_0)}{\chi_l(n_0 k a_0)} = \frac{\psi_l'(n_s k a_0)}{\psi_l(n_s k a_0)}$$

$$\eta_s = \begin{cases} \frac{n_0}{n_s}, & TE\ modes \\ \frac{n_s}{n_0}, & TM\ modes \end{cases} \qquad (3.1)$$

Equation (1) is the characteristic equation of solid glass microsphere resonator. Functions ψ_l and χ_l are the spherical Ricatti-Bessel function and the spherical Ricatti-Neumann function, respectively.

Table 1 Parameters of Solid Glass Microsphere and PWHGM Models

Microsphere types and parameters		
	Solid glass microsphere	**Porous wall hollow glass microsphere**
Diameter	$a_1 = a_0$	$a_1 = a_0 + h$
Porous wall Thickness	0	h
Refractive index (RI)	$n_s = 1.45, n_0 = 1.0$	$n_p = 1.45, n_s = n_0 = 1.0$
Sensitivity	$(S_0)_{TE}, (S_0)_{TM}$	S_{TE}, S_{TM}
Wave vector (before RI change)	k_0	k_0
Electric field (before RI change)	T_0	T_0
Resonance wavelength	λ_R	λ_R

Resonant wave number is shown as $k=2\pi/\lambda_R$. The characteristic equation for PWHGM can be expressed as [98, 101-103]:

$$\eta_0 \frac{\chi_l'(n_0 k a_1)}{\chi_l(n_0 k a_1)} = \frac{B_l \psi_l'(n_p k a_1) + \chi_l'(n_p k a_1)}{B_l \psi_l(n_p k a_1) + \chi_l(n_p k a_1)}$$

$$B_l = \frac{\eta_p \, \psi_l'(n_s k a_0)\chi_l(n_p k a_0) - \psi_l(n_s k a_0)\chi_l'(n_p k a_0)}{\psi_l'(n_p k a_0)\psi_l(n_s k a_0) - \eta_p \, \psi_l(n_p k a_0)\psi_l(n_s k a_0)}$$

$$\eta_0 = \begin{cases} n_0/n_p, & TE\ modes \\ n_p/n_0, & TM\ modes \end{cases}$$

$$\eta_p = \begin{cases} \dfrac{n_s}{n_p}, & TE\ modes \\ \dfrac{n_p}{n_s}, & TM\ modes \end{cases} \qquad (3.2)$$

In equation (2), prime denotes the derivative of a function by its argument and there is an exponential decay in the exterior solution at resonance. Given the angular mode l, a series of λ_R, ka_0 and ka_1values satisfy the characteristic equations (1) and (2), which are referred as the first-order mode, the second-order mode, and the third-order mode, etc. In chemical vapor sensing simulation, the increasing effective refractive index δn_p is considered and a resonance wavelength shift occurs accordingly. In the simulation modeling, the PWHGM wall thickness has a threshold, beyond which the PWHGM model can be simplified as a solid porous glass sphere to achieve the highest sensitivity and the best sensing characteristics. When $h > h_0$, WGMs are mainly confined inside the porous wall, and the characteristic equation of PWHGM can be simplified to be the same as solid glass sphere characteristic equation, thus, the PWHGM can be simplified to an

ideally homogenous porous silica microsphere of radius a_1 and refractive index $n_s = n_p = 1.45$, as shown in Fig 3.1 (a).

3.2.2 Simulation of Porous Glass Sphere Resonator Sensitivity

The effective RI change sensitivity at the interface of the microresonator and surroundings can be given by [98, 101-103]:

$$S = \frac{\delta\lambda_R}{\delta n} = -\frac{\lambda_R}{\delta n}\cdot\frac{\delta k}{k_0}$$

$$\delta n = \begin{cases} \delta n_0, & Solid\ glass\ sphere \\ \delta n_p, & PWHGM \end{cases} \qquad (3.3)$$

For solid glass microsphere, different forms of $\delta k/k$ is given in TE and TM modes respectively [101-103]:

$$\left(\frac{\delta k}{k}\right)_{TE} = -\frac{\delta(n_0^2)\int_0^\infty T_0^2(r)dr}{2\int_0^\infty [n(r)T_0^2(r)]dr}$$

$$\left(\frac{\delta k}{k}\right)_{TM} = -\frac{\delta(n_0^2)\left[-T_0(a_0)T_0'(a_0^+) + n_0^2k_0^2\int_{a_0}^\infty T_0^2(r)dr\right]}{2n_0^4k_0^2\int_0^\infty T_0^2(r)dr}$$

$$n(r) = \begin{cases} n_s, & r < a_0 \\ n_0, & r > a_0 \end{cases}$$

$$T_0(r) = \begin{cases} \psi_l(n_s kr), & r < a_0 \\ D_l\chi_l(n_0 kr), & r > a_0 \end{cases}$$

$$D_l = \psi_l(n_s ka_0)/\chi_l(n_0 ka_0)$$

$$\delta(n_0^2) \approx 2n_0\delta n_0, \quad when\ \ \delta(n_0^2) \ll 1 \quad (3.4)$$

Using equation (4) in the equation (3), the sensitivity can thus be expressed as [98, 101-103]:

$$(S_0)_{TE} = \frac{n_0 \lambda_R I_0}{n_s^2 I_s + n_0^2 I_0}$$

$$(S_0)_{TM} = \frac{\lambda_R^2 [n_0 k_0 I_0 - D_l^2 \chi_l(n_0 k_0 a_0) \chi_l'(n_0 k a_0)]}{2\pi n_0^2 (I_s + I_0)}$$

$$I_s = \int_0^{a_0} [\psi_l(n_s k_0 r)]^2 dr$$

$$I_0 = \int_{a_0}^{\infty} [D_l \chi_l(n_0 k_0 r)]^2 dr \qquad (3.5)$$

Compared to solid glass microsphere, the PWHGM shows a more complicated form as the RI of the porous silica shell with thickness h of should be considered. Thus, the forms of *δk/k* in TE and TM modes are shown as [98, 101-103]:

$$\left(\frac{\delta k}{k}\right)_{TE} = -\frac{\delta\left(n_p^2\right) \int_{a_0}^{a_1} T_0^2(r) dr}{2 \int_0^{\infty} [n(r) T_0^2(r)] dr}$$

$$\left(\frac{\delta k}{k}\right)_{TM} = -\frac{\delta(n_0^2) \left[T_0'(a_1) T_0'(a_0^-) - T_0(a_0) T_0'(a_0^+) + n_p^2 k_0^2 \int_{a_0}^{\infty} T_0^2(r) dr\right]}{2 n_p^4 k_0^2 \int_0^{\infty} T_0^2(r) dr}$$

$$n(r) = \begin{cases} n_s, & r < a_0 \\ n_p, & a_0 < r < a_1 \\ n_0, & r > a_1 \end{cases}$$

$$T_0(r) = \begin{cases} A_l \psi_l(n_s k r), & r < a_0 \\ B_l \psi_l\left(n_p k r\right) + \chi_l\left(n_p k r\right), & a_0 < r < a_1 \\ C_l \chi_l(n_0 k r), & r > a_1 \end{cases}$$

$$A_l = \frac{B_l \psi_l\left(n_p k\, a_0\right) + \chi_l\left(n_p k\, a_0\right)}{\psi_l(n_s k\, a_0)}$$

$$C_l = \frac{B_l \psi_l\left(n_p k\, a_1\right) + \chi_l\left(n_p k\, a_1\right)}{\chi_l(n_s k\, a_1)}$$

$$\delta\left(n_p^2\right) \approx 2n_p\delta n_p, when\ \ \delta\left(n_p^2\right) \ll 1 \qquad (3.6)$$

In PWHGM resonator, the chemical sensing equation is given using equation (3.3) and (3.6) with TE and TM modes, respectively [98, 101-103]:

$$S_{TE} = \frac{n_p\lambda_R I_p}{n_s^2 I_s + n_p^2 I_p + n_0^2 I_0}$$

$$S_{TM} = \frac{\lambda_R^2 \begin{bmatrix} n_s n_0 k_0 I_p + n_s C_l^2 \chi_l(n_0 k_0 a_1)\chi_l'(n_0 k_0 a_1) \\ -n_0 A_l^2 \psi_l(n_s k_0 a_0)\psi_l'(n_s k_0 a_0) \end{bmatrix}}{2\pi n_s n_0 n_p\left(I_s + I_p + I_0\right)}$$

$$I_s = \int_0^{a_0} [A_l\psi_l(n_s k_0 r)]^2 dr$$

$$I_0 = \int_{a_1}^{\infty} [C_l\chi_l(n_0 k_0 r)]^2 dr$$

$$I_p = \int_{a_0}^{a_1} \left[B_l\psi_l\left(n_p k_0 r\right) + \chi_l\left(n_p k_0 r\right)\right]^2 dr \qquad (3.7)$$

For the adsorption of chemical vapor molecules at the surface of the solid glass microsphere or into the porous channels of the PWHGM, the corresponding effective RI change results in the WGMs propagation optical path extension. Therefore, the TE and TM resonances shift with different wavelength range and shows diverse sensitivity response.

In computational modeling, the PWHGM modeling is demonstrated rather than the solid glass sphere. Because both types of spheres follow a similar simulation step and solid glass microsphere resonator was shown with a relatively low sensitivity compared to the PWHGM resonator [105].

In the simulation, first, varied sizes of PWHGMs with different sensitivity are demonstrated. Fig. 3.2 shows the sensitivity change of different sizes PWHGMs resonators in the fundamental TE modes as a function of wall thickness. PWHGMs with an increasing size are simulated with radius of 23 µm, 28 µm, 33 µm and 38 µm, respectively. The sensitivity increases as the porous wall gets thicker. The sensitivity of resonators in all sizes turns out to be in the same level when the sphere porous wall is thicker than 2 µm, which is the proposed wall thickness threshold for PWHGM resonator model simplification in modelling section. In practice, the PWHGM with diameter of 76 µm was tested in the experiment. Thus, the simulation focuses on this specific size and investigated the porous wall thickness effect as well as its modes.

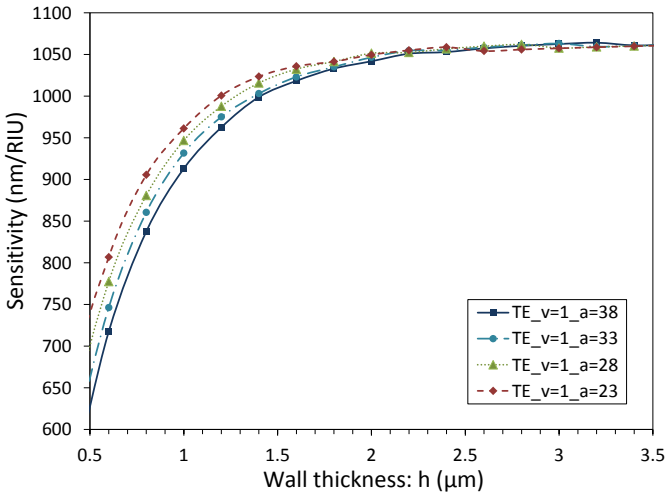

Fig. 3.2. The chemical sensitivity of TE modes in PWHGM resonator at different sphere sizes as a function of porous wall increase [104].

Figure 3.3 gives the sensitivity variation trend of the 76 µm PWHGM under different wall thicknesses in several modes. The parameter a in the figure legend is the radius of the microsphere. First-order and second-order of TE and TM modes are shown

with different sensitivity. The figure demonstrates the increasing trend of sensitivity when the porous wall is getting thicker under different modes. For the first order modes, the highest increasing slope exists at the wall thickness between 1 μm and 2 μm. The sensitivity of first order modes stabilizes when the porous wall is thicker than 2 μm. The stability of second order occurs after 3 μm. The inset of Fig. 3.4 shows the actual wall thickness of the PWHGM. The fundamental TE and TM modes with v = 1 always provide a higher sensitivity comparing to higher order.

In Fig. 3.3, the wall thickness in nanometre scale is also considered compared to Fig. 3.2. The fundamental modes of TE and TM show a high sensitivity increase from 500nm to 1μm wall thickness. However, the second-order TE and TM modes do not even exist in that wall thickness range. Meanwhile, the fundamental TE mode shows a higher sensitivity than the fundamental TM mode in nanoscale wall thickness. Thus, the first order TE mode of PWHGM resonator is used to compare with the experiment.

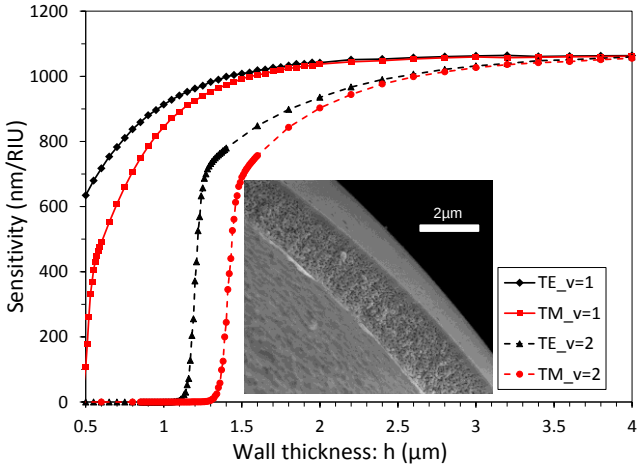

Fig. 3.3. PWHGM resonator chemical sensitivity change as a function of porous wall increase in TE and TM modes. The solid black curve is the first order TE mode; the solid red curve is first order tm curve; the dashed black curve is second order TE mode and the dashed red curve is second order TM mode [104].

3.2.3 Comparison of Experimental and Simulation Results

From Fig. 3.4 it can be seen that the simulation results agree well with the sensitivity increasing trend of the experiment data. The reason for a lower sensitivity in the experiment is that that acetone vapor may be diluted during the storage or transmission stage.

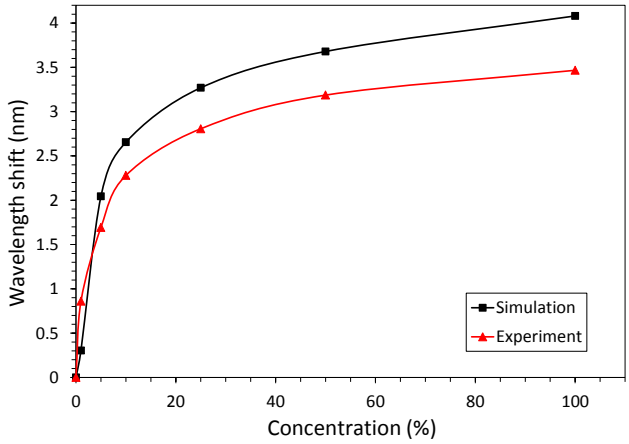

Fig. 3.4. Simulation and experiment of PWHGM resonator for chemical vapor detection sensitivity. Black curve with square marker is the simulation and red curve with triangle marker is the experiment [104].

Computational model reveals the essence of molecular adsorption caused refractive index change on the sphere surface of a solid glass sphere and through the porous channels of a PWHGM. The computational simulation agreed well with the experimental results in the sensing trend. It is expected that the experimentally verified optical microresonator model can be used for prediction and optimization of the resonator for high sensitive chemical vapor detection.

CHAPTER FOUR

FIBER PIGTAILED THIN WALL COUPLED OPTICAL RESONATOR

4.1 Introduction of Optical Resonator Excitation Methods

Efficiently coupling light into and out of an optical microstructure is one of the most important steps in the study and application of WGM resonators. Different methods have been investigated to excite a WGM resonator through evanescent fields, including prisms, pedestal waveguides, side-polished optical fibers, angle-polished fiber tips, and fiber tapers [1, 5, 20, 79, 106-110]. By phase-matching the evanescent waves at the internal surface of a prism with the WGMs, light can be coupled into a microresonator [1]. Prism coupling is flexible and efficient. However, it is bulky and inconvenient in practical applications [106]. On-chip pedestal structures have been demonstrated for efficiently and reliably coupling light into a microsphere resonator [107]. However, the pedestal waveguide has a complicated structure and requires high fabrication precision. From the application perspective, fiber pigtailed couplers are preferred because of the convenience in light source coupling and signal detection. Side-polished optical fibers [108, 109] and angle-polished fiber tips [110] have been used to excite high-Q microsphere resonators. However, these two fiber couplers have shown low coupling efficiency. The side-polished optical fiber couplers were efficient (up to 20%, defined as the ratio between the power injected into a specific mode and the power carried by the coupler) for microspheres with a large diameter (~1 mm in diameter) and much less efficient for small resonators. The angle-polished fiber tip had an efficiency of about

60%. Perhaps the most efficient fiber optic coupler is a fiber taper with a diameter less than 2 μm [5]. However, fiber tapers are fragile and sensitive to environmental perturbations.

4.2 Development of Fiber Pigtailed Thin Wall Coupler

In this chapter, we report a new robust coupler for excitation of the WGMs of microsphere resonator. The coupler has a fiber pigtail for convenient connection to a light source and a photodetector (or an optical spectrum analyzer). The microsphere resonator is dropped into and in contact with the thin-wall capillary tube. Light coupling into the resonator is through the evanescent fields of the capillary wall. As a result, the coupling is not only alignment-free but also mechanically robust.

4.2.1 Optical Fiber and Capillary Tube

A flexible fused silica capillary tube (FFSCT) (Polymicro Technologies, LLC) was used to fabricate the coupler. The capillary tube has an inner diameter of 75 μm, an outer diameter of 150 μm, and a wall thickness of 37.5 μm. The FFSCT was fusion spliced to a multimode optical fiber (Fiber Instrument Sales, INC 62.5/125). The arc power and duration of the fusion splicer (Sumitomo T-36) were adjusted to obtain a cone-shape connection between the fiber and the capillary as shown in Fig. 4.1(a). A microsphere was then fed into the capillary tube till it stopped at the bottom of the conical area and was stably held by the capillary wall as shown in Fig. 4.1(c). The microspheres used in this study were provided by MO-SCI Corporation, consisting of a distinct silica-

rich and sodium borate phase with a solid morphology. The diameter of the glass microspheres ranged from 50 to 75 μm, which could be easily inserted into the capillary.

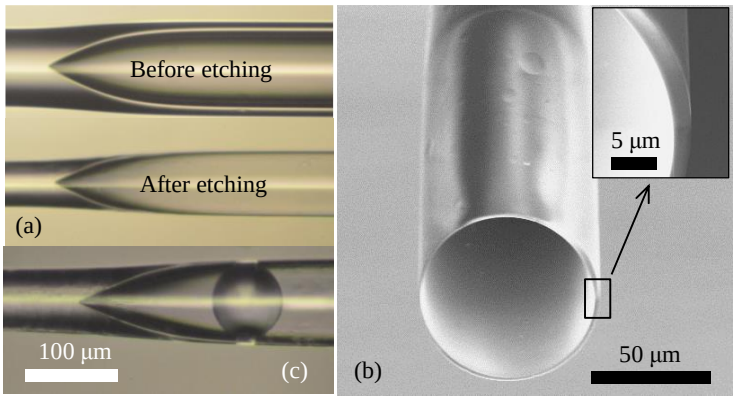

Fig. 4.1. Microscopic images of the fiber pigtailed thin wall capillary coupler at various fabrication steps. (a) Before and after etching, (b) SEM image of the etched capillary wall with a thickness of about 2 μm, (c) Etched capillary with a microsphere inserted [111].

4.2.2 Chemical Etching

After placement of the microsphere, the opening end of capillary cavity was sealed by fusion splicing it to a short section of optical fiber. Hydrofluoric (Acros Organics, 20%) acid was then to etch and reduce the thickness of the capillary wall. The wall thickness of the capillary was controlled during the etching process by varying etching duration. Upon reaching the desired wall thickness, the etched capillary can be opened by cleaving to allow the encapsulated microsphere to access the environment for sensing applications.

Figure 4.1 shows a set of images of the fiber pigtailed coupler during the various steps of fabrication. Fig. 4.1(a) shows the microscopic images of the structure before and after etching. Fig. 4.1(b) shows the scanning electron microscopy (SEM) image of the

etched capillary wall with the wall thickness estimated to be about 2 μm. The final assembled WGM resonator structure is shown in Fig. 4.1(c), where the microsphere is held by the etched capillary wall.

4.2.3 Thin Wall Capillary Waveguide Field Distribution

To verify the waveguide capability of the etched capillary wall, the near-field power distribution of the fiber pigtailed coupler was measured using a setup as shown in Fig. 4.2(a). The capillary was fusion spliced to a multimode fiber, etched to have a wall thickness of about 5 μm, and cleaved to a length of about 300 μm. A tunable laser at the wavelength of 1550 nm was connected to the multimode fiber as the source. An end-cleaved single mode fiber with a core diameter of 3 μm (Fibercore SM450) was mounted on a three dimensional translation stage and positioned at a distance of about 20 μm from the cleaved end face of the capillary. The other end of the single mode was connected to an optical power meter. Via computer control, the single mode fiber scanned through the area to map the near-field power distribution of the coupler structure.

Figure 4.2(b) shows the measured line-scan power distribution profile across the center of the capillary tube as shown in the inserted SEM image. The distance between the two power intensity peaks was measured to be 79 μm, which agreed well with the dimension of the thin capillary. The power distribution measurement indicated qualitatively that majority of power was guided through the capillary wall.

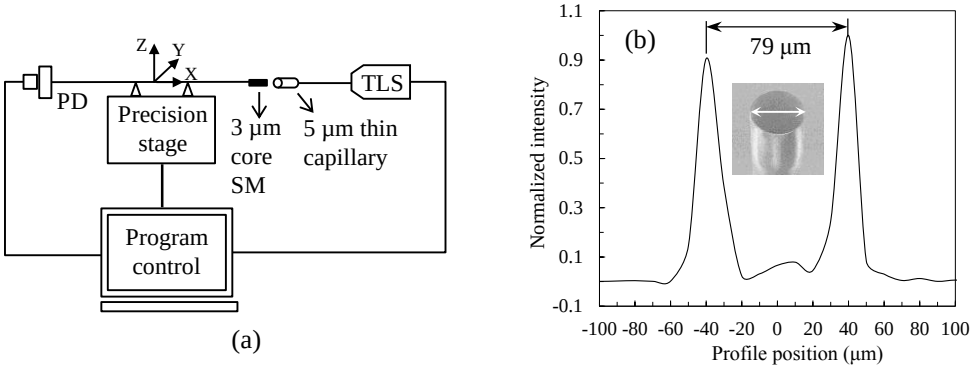

Fig. 4.2. Measurement of the near-field power distribution of the fiber pigtailed thin wall capillary waveguide. (a) Schematic of the near-field power distribution measurement system, (b) Line-scan power distribution profile [111].

Optical beam propagation using RSoft was applied to analyze the field intensity distribution with capillary wall thickness change. In Fig. 4.3, two structures with different wall thickness were demonstrated with field distribution along the wave propagation. When the wall was 15 µm, majority of the intensity was confined within the capillary wall. The intensity power tails started to "leak" out of the capillary wall boundaries, especially in the cone shape area. This amount of power propagating in free space can be applied for the coupling of optical microresonators.

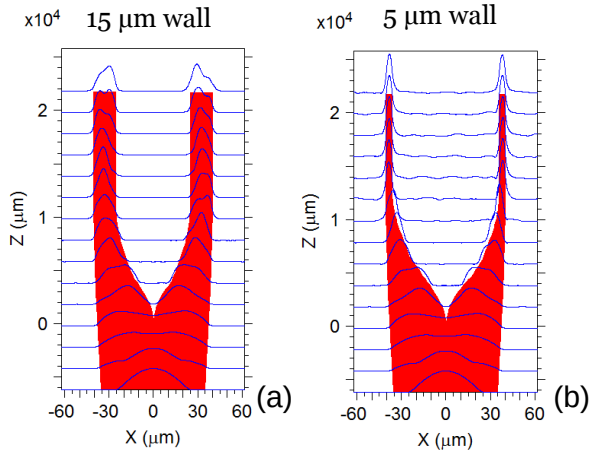

Fig. 4.3. RSoft simulation of beam propagation with different wall thicknesses: (a) 15μm and (b) 5 μm.

4.3 Thin Wall Capillary Coupled Microsphere Resonator

4.3.1 Excitation Schematics

Figure 4.4 shows the schematic structure of the fiber pigtailed thin wall capillary coupled microsphere resonator as well as the experiment setup to interrogate the resonator. The coupler is made by fusion splicing a capillary tube to an optical fiber. The arc power of fusion is controlled so that a cone shape is formed at the connection of the fiber and the tube. The structure is then chemically etched to reduce the capillary wall thickness to a few microns. A microsphere can be dropped into the thin wall capillary tube from the opening. It stops at the cone shape, being in contact with the inside wall of the etched capillary tube.

To interrogate the resonator, the light from a tunable laser source (Agilent 8168F) passes through a 3dB fiber coupler, splits at the cone shape into the wall of the etched capillary, a certain portion of the evanescent wave was coupled into the microsphere to excite the WGMs. The WGMs are coupled back to the capillary wall in the opposite side. The light propagates backwards to the optical fiber through the cone shape, and can be detected by a photodetector (Agilent 8163A). By scanning the wavelength of the tunable laser source, the resonance spectrum is recorded. The circular periphery of the microsphere is in contact with the etched capillary wall. Therefore, multi-paths of WGMs can be excited.

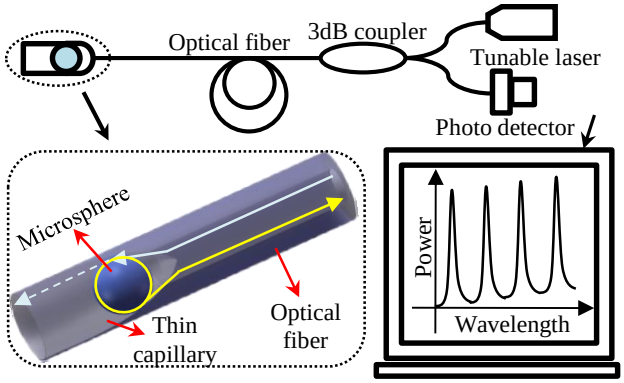

Fig. 4.4. Schematic of the fiber pigtailed thin wall capillary coupled whispering gallery modes microresonator and interrogation setup [111].

4.3.2 Coupling Efficiency and Wall Thickness Dependency

The effect of wall thickness on WGM excitation has also been investigated experimentally. The glass microsphere used in the experiments had a diameter of 68 µm. During the etching process, the structure was pulled out from the etching liquid every minute, cleaned and dried. The wall thickness was then measured using a measuring optical microscope (Nikon MC-203) and the reflection spectrum of the resonator structure was recorded using the setup shown in Fig. 4.4.

Figure 4.5(a) shows the recorded reflection spectrum of the resonator at the etching times of 0, 15, 20, 25, 25.5 and 26 minutes, respectively. The wall thicknesses at these time intervals, estimated based on the assumption of a constant etching rate, were 37.5, 12, 8, 4, 2 and < 1 µm, respectively. At the etching time of 15 minutes, the spectra started showing periodical coupling and the average intensity increased by 3 dB compared to the original structure before etching. At the etching time of 20 minutes, the periodical spectra were observable. At the etching time of 25 minutes, the coupling strength reached its peak value and the resonance became obviously periodic. At the

etching time of 26 minutes, the resonance disappeared and the average reflection intensity dropped significantly, indicating that the capillary tube was etched through.

Figure 4.5(b) shows the calculated Q-factor and peak intensity of the resonance as a function of etching time, where both the Q-factor and peak intensity increased drastically when the wall thickness decreased to a few microns after 20 minutes of etching. However, when the etching time passed 25 minutes, both the Q-factor and peak intensity dropped. In addition, the periodical spectra began to diminish. The experiment clearly showed the under coupling, critical coupling and over coupling when the wall thickness changed as the etching process progressed.

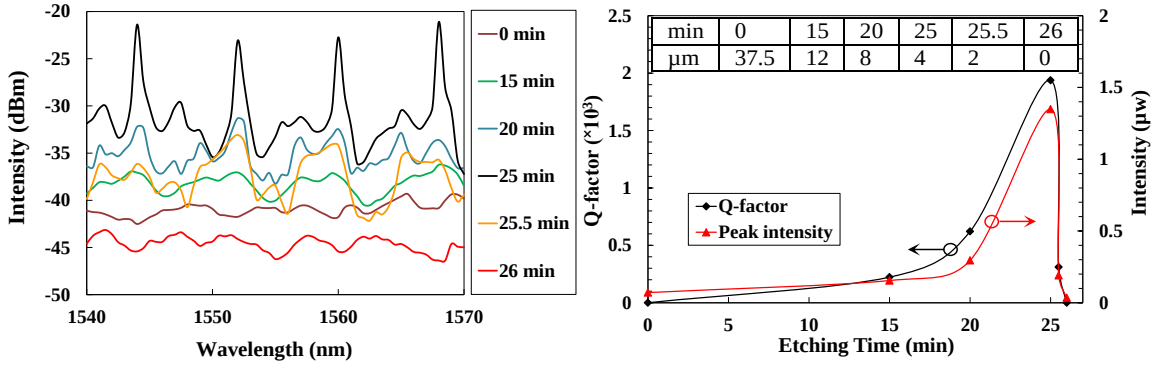

Fig. 4.5. Progress of coupling as a function of etching time. (a) Reflection resonance spectrum at various etching times, (b) Resonance Q-factor and peak intensity as a function of etching time. Inset table, the wall thickness estimated based on etching time [111].

4.3.3 Reflection Resonance Spectrum and Analysis

Figure 4.6 shows the reflection spectrum of a fiber pigtailed thin wall capillary coupled microsphere resonator with a diameter of 71 μm in air. The wall thickness was determined to be about 5 μm based on the SEM image. The spectrum shows a clear

pattern of periodic resonant peaks. In addition to the strongest set, other set of resonance peaks are also identifiable. As shown in Fig. 4.6, the Q-factor of the dominant resonance, at the resonant wavelength of 1535.114 nm, has a full width at half maximum (FWHM) of 0.134 nm. The Q-factor was calculated to be 1.14×10^4 and the free spectrum range (FSR) was 7.25 nm.

Light coupling from the capillary wall into the microsphere is similar to the case of using tapered fiber as the coupler whose propagation constant matches that of the WGMs. The wall thickness used in our experiment was about 5 μm, which was larger than the typical diameter of commonly used fiber tapers. We expect that the lowest radial mode number (n = 1) WGM was preferentially excited [5]. The group index n_g of the lowest radial mode number WGM can be estimated using the following equation [1, 87]:

$$n_g = \frac{\lambda_1 \times \lambda_2}{2\pi R \times FSR} \qquad (4.1)$$

where λ_1 and λ_2 correspond to the adjacent resonance peak wavelengths and R is the microsphere radius. Using the data shown in Fig. 4.6, the effective group index was calculated to be 1.496, which was close to the index (1.47-1.51) of the microsphere material (borosilicate glass) [112], suggesting that the fundamental mode ($n = l$, $l = |m|$) was excited. The corresponding mode order numbers are provided in Fig. 4.6.

When an optical fiber taper is used to excite a microsphere resonator, light coupling is mainly in single orbital plane. The etched capillary wall coupler described here can couple light into a microsphere in many orbital planes along the circular peripheral contact between the microsphere and the capillary wall. Because the

microsphere usually has an imperfect sphericity, multiple set of resonance peaks are expected, as seen in Fig. 4.6. The Q-factor of the capillary wall coupled microresonator observed in our experiments was lower than that excited by a fiber taper. The low Q-factor may be attributed to several reasons. First, the fundamental modes excited in different orbital planes may have slightly different optical paths. As a result, the actual FWHM might be broadened. Second, the solid microspheres used in the experiments were made of borosilicate glass which has higher optical loss compared with the fused silica microspheres. Third, the microsphere was in contact with the capillary wall.

As result, the coupling was not at the highest efficiency position where the excitation waveguide should be placed at a slight distance (about 300 nm) from the resonator [113]. The contribution mechanisms of these and other possible reasons deserve a detailed study and will be the subject of further research.

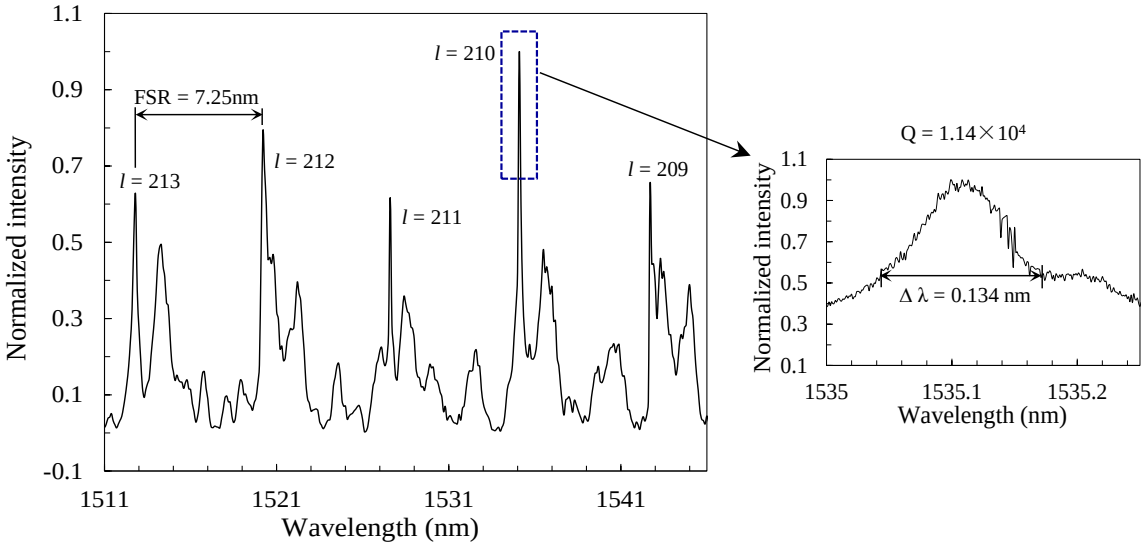

Fig. 4.6. Reflection spectrum of the thin wall capillary coupled microsphere resonator in air, with mode identification numbers. Inset: Zoom-in spectrum of the resonance peak [111].

On the other hand, the thin wall capillary contact-type coupler provides a robust support for the microsphere resonator. The microresonator and the coupler are well-integrated and mechanically stable.

In summary, we have demonstrated a fiber pigtailed thin wall capillary structure for excitation of WGM microsphere resonators. Light coupling is through the circular peripheral contact between the microsphere and the supporting capillary wall. By etching the capillary wall to a thickness of a few microns and using a borosilicate glass microsphere as the resonator, periodical resonance spectrum was observed with a Q-factor of 1.14×10^4.

The coupling conditions as a function of the wall thickness have been experimentally studied showing the under coupling, critical coupling and over coupling as the wall thickness reduced. The coupler operates in the reflection mode and provides a robust mechanical support to the microsphere resonator. It is expected that the new coupler may find broad applications in WGM resonator based sensors, optical filters and lasers.

CHAPTER FIVE

CONVENIENT PROBE FOR SENSING AND LASING APPLICATIONS

5.1 Integration of Porous Glass Microsphere with the Thin Wall Capillary

Thin wall capillary was proven as an efficient waveguide for the integration of optical microresonator. In addition to further extend its sensing efficiency, here we show a convenient chemical sensor probe using porous glass microsphere (PGM) optical microresonator coupled by the fiber pigtailed thin wall waveguide. The evanescent field along the surface of the capillary inner wall couples to the PGM and a multi-path spherical microresonator is realized. Surrounding chemical vapor adsorbed by the porous channels leads to a refractive index change and then a resonance wavelength shift is quantified. The porous structure of the PGM enhances the adsorption of chemical vapor molecules; consequently, the interaction between the molecule and the WGMs circulating inside the resonator is boosted. The multi-directional and supportive structure ensures the sensor robustness. Together with the porous structure, the robustness of the sensor realizes a convenient, in-situ, highly sensitive chemical sensor probe.

5.2 Convenient Chemical Sensor Probe

5.2.1 Chemical Sensor Probe Sensing Principle

Figure 5.1 demonstrates the schematic of the chemical sensing using the thin wall waveguide excited PGM resonator. First, the PGM is coupled by the input light and a WGMs resonator is realized, shown as the red circle near the PGM inner surface in Fig.

5.1(a). Second, the chemical vapor enters the capillary cavity and fully fills the porous channels of the PGM (in Fig. 5.1(a), shown as the orange color arrows through the PGM), changes the effective refractive index of the PGM and leads to a wavelength shift in the output resonance signal. The micro window provides a free path for the chemical vapor flow. In Fig. 5.1(b), the worn-shape porous structure of the PGM provides enough nano-scale pores for the molecules and enhances the chemical vapor adsorption. Comparing to solid microsphere, which interacts with the chemical at the sphere surface, the PGM fully adsorbs the chemical vapor molecules into the sphere shell and further changes the PGM refractive index. The opening of the capillary cavity in Fig. 5.1(c) offers sufficient access for the incoming chemical.

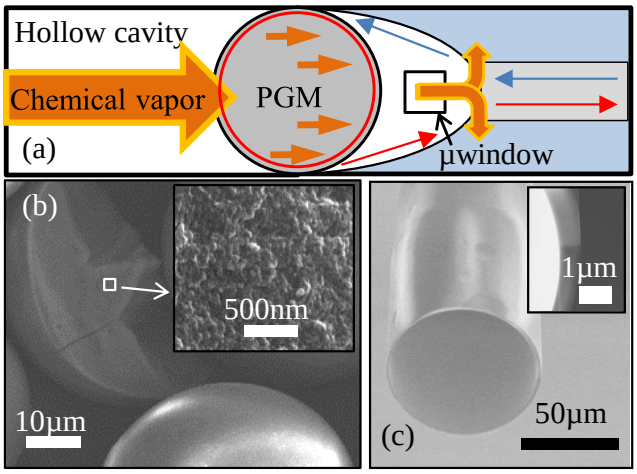

Fig. 5.1. Optical microresonator chemical sensor probe: (a) chemical vapor flow path in the sensor probe; (b) SEM of the porous structure of the PGM; (c) the cross section of the capillary wall.

Figure 5.1 demonstrates the schematic of the chemical sensing using the thin wall waveguide excited PGM resonator. First, the PGM is coupled by the input light and a WGMs resonator is realized, shown as the red circle near the PGM inner surface in Fig.

5.1(a). Second, the chemical vapor enters the capillary cavity and fully fills the porous channels of the PGM (in Fig. 5.1(a), shown as the orange color arrows through the PGM), changes the effective refractive index of the PGM and leads to a wavelength shift in the output resonance signal. The micro window provides a free path for the chemical vapor flow. In Fig. 5.1(b), the worn-shape porous structure of the PGM provides enough nano-scale pores for the molecules and enhances the chemical vapor adsorption. Comparing to solid microsphere, which interacts with the chemical at the sphere surface, the PGM fully adsorbs the chemical vapor molecules into the sphere shell and further changes the PGM refractive index. The opening of the capillary cavity in Fig. 5.1(c) offers sufficient access for the incoming chemical.

5.2.2 Chemical Sensing Setups and Tests

The chemical sensing setup is schematically shown in Fig. 5.2. The light from the tunable laser source (HP-8168F) transmits through the multimode optical fiber (Fiber Instrument Sales, INC 125/62.5) and 50/50 coupler, and then launches at the cone-shape area of the thin capillary cavity. Then the light splits into multiple optical paths and propagates along the capillary thin wall, shown as the light blue line along the capillary structure in Fig. 5.2 (a). A certain portion of the evanescent wave couples into the PGM to excites the WGMs, shown as the yellow color circular along the surface of the PGM in Fig. 5.2 (a). Then the WGMs couples back to the capillary wall in the opposite side. The light propagates backward to the optical fiber through the cone-shape and detected by the photodetector (Agilent 8163A). Multi-paths of WGMs are excited due to the circular

periphery of the microsphere in contact with the capillary inner wall. The resonance spectrum periodical peaks can thus be obtained by scanning the wavelength of the tunable laser.

In chemical sensing test, the probe is placed inside a stainless steel (SS) tube chamber. The ethanol vapor concentration is adjusted by changing the mixture portion between pure nitrogen gas and ethanol vapor in the SS chamber.

The chemical molecules adsorbed by the porous channels of the microsphere lead to a certain refractive index change, shown as Fig. 5.2 (b). A relative resonance wavelength shift can be monitored and recorded by a programmable controlled optical spectrum analyzer (Ando AQ6319).

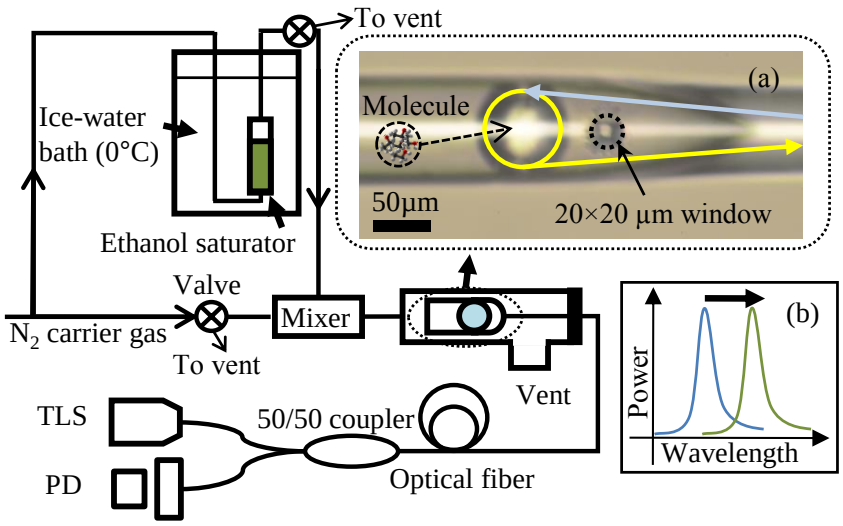

Fig. 5.2. Schematic of thin wall capillary coupled porous glass microsphere resonator for chemical sensing. TLS: tunable laser source, PD: photodetector. (a) Chemical sensor probe with fs laser fabricated micro-window and (b) wavelength shift with increasing ethanol vapor concentration.

5.2.3 Porous Glass Microsphere and Integration with Thin Wall Coupler

In this experiment, the fabrication of the thin wall capillary coupler is demonstrated in previous chapters. After the complete fabrication of thin wall coupler, a PGM was dropped into the capillary tube until it stopped at the conical area and stably held by the capillary wall as shown in Fig. 5.2(a).

The MO-SCI Corporation provided the PGMs in the experiment. PGMs are composed of a chemically stable sodium borosilicate glass material constructed in the form of a tortuous network of nanometer-scale channels. The glass is heat treated and drawn by a leaching process to produce interconnected pores or channels. The PGMs range from 50 μm to 75 μm in diameter. The pore diameter ranges from 20 nm to 200 nm. The size of the porous channels ensures the molecule adsorption and the supportive circular structure guarantees the robustness of the probe.

5.2.4 Femtosecond Laser Micro-window Fabrication

The micro window in Fig. 5.2(a) was created by a lab-integrated femtosecond laser (fs) 3D micro machining system with a regeneratively amplified Ti: Sapphire fs laser (Coherent, Inc.). The repetition rate, center wavelength, and pulse width of the femtosecond laser were 250 kHz, 800 nm, and 200 fs, respectively. The initial maximum fs laser output of 0.8 w was attenuated down to 120 mw using a combination of laser beam optics, halfwave plates, polarizer and neutral density filters for the objective of higher precision fabrication [114]. The dimension of the window was 20 by 20 μm square. Because the capillary exhibits a multi-path coupling to the PGM, then the micro window

interruption slightly impairs the overall coupling efficiency. The fs laser fabricated micro window assures the unobstructed chemical flow path from the tube opening through the PGM porous channels until across the micro window, and the vapor saturation effect in the cavity is alleviated. Thus, the sensor lifetime extends for multiple tests.

5.2.5 Resonance Spectrum of Porous Glass Microsphere Resonator

Figure 5.3 shows a reflective resonance spectrum of a PGM resonator with a diameter of 72 μm under room temperature. The wall thickness was determined to be about 2 μm based on the SEM image. The spectrum shows a clear pattern of periodic resonances. The Q-factor of the 72 μm PGM resonator was calculated to be 1.38×10^3 at the resonant wavelength of 1599.48 nm. The corresponding full width at half maximum (FWHM) was 1.16 nm and the free spectrum range (FSR) was 7.61 nm. The mode order numbers are provided in Fig. 5.3.

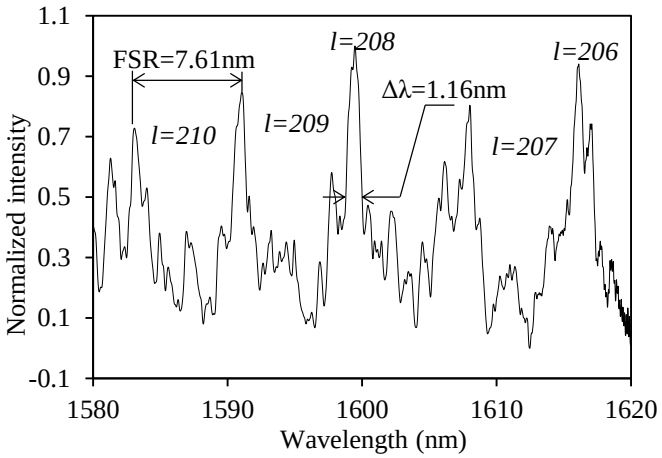

Fig. 5.3. Reflection resonance spectrum of the PGM resonator coupled by thin wall capillary.

The Q-factor is relatively lower than the resonator coupled by fiber taper [113]. This can be attributed to several aspects. First, the porous structure of a PGM introduced higher scattering loss compared to solid silica glass. Second, the contact coupling approach was not the best option for high efficiency coupling, in which the excitation waveguide should be at a certain distance (~300 nm) from the resonator [113]. Though the Q was degraded due to the porous structure induced scattering loss, however, this porous channel structure with high adsorption rate makes PGM resonator a useful chemical vapor sensor. Because chemical vapor molecules smaller than the sizes of the pores can be easily adsorbed to the resonator and therefore detected by measuring the subsequent resonance wavelength shift.

Meanwhile, the capillary coupler demonstrated a coupling structure with relatively higher robustness than fiber taper. As a result, the thin wall capillary coupled PGM microresonators shall provide high sensitivity for chemical sensing with improved robustness for potential field tests.

5.3 Sensor Probe Chemical Vapor Response

Figure 4 shows the chemical sensing results based on the thin wall capillary coupled PGM optical resonator sensor probe. Experiments were performed by monitoring the resonance peak responded to the increasing concentrations of ethanol (sigma-aldrich, $\geqslant$99.8%) vapors. In the experiment, a 57 μm PGM was tested and the capillary coupled PGM resonator sensor probe was horizontally placed in a chemical vapor chamber, which consist of gas supply and vent system as shown in Fig. 5.2. The ethanol solution was

filled in the ice bubbler and nitrogen gas was served as the carrier under the control of a flow meter valve. The ethanol vapor concentration was calculated based on the vapor pressure at 0 °C and the diluting gas flow rate. The tests were performed at local atmospheric pressure and room temperature.

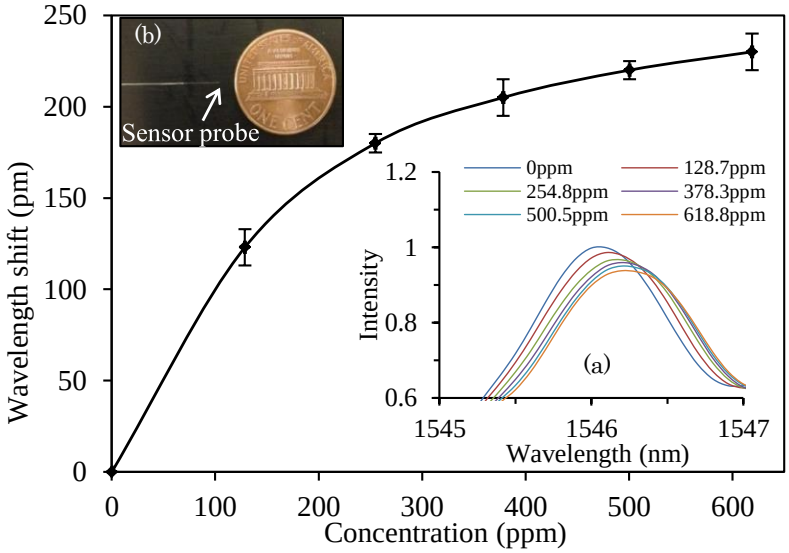

Fig. 5.4. Sensor response to ethanol vapor concentration change in N2 gas carrier. Insets: (a) resonance spectrum shift with ethanol concentration increase and (b) the dimension comparison between the sizes of the sensor probe and a one-cent coin.

In the experiment, the tested vapor concentration was set at 0 ppm, 128.7 ppm, 254.8 ppm, 378.3 ppm, 500.5 ppm and 618.8 ppm, respectively. The sensor resonance responses to ethanol vapor concentration are shown in Fig. 5.4 (a), from which can be seen that the increasing ethanol vapor results in a resonance shift towards longer wavelength. Curve-fitting of the resonance was done to minimize the random intensity noises. In each set of test, the sensor probe exhibited an ultra-fast response time for less than one second. The chemical sensor probe responded monotonically to vapor

concentration change and provided an obvious correlativity for quantitative measurement. A parabolic relationship between the ethanol vapor concentration and resonance wavelength shift is shown in Fig. 5.4. This is because the adsorption of molecule into the porous channels is nonlinear. Fig. 5.4 (b) shows the volume comparison between the miniature size of the sensor probe and the size of a penny.

During the chemical vapor tests, the multi-directional WGMs coupling scheme fully extended the interaction area between the sensor and the surroundings. Compared to the single dimensional coupling using fiber taper, the fragility nature of fiber taper was improved by using a relatively robust capillary wall as the coupler and the resonator supporter.

In this section, we have shown an innovative miniaturized chemical sensor based on thin wall capillary coupled porous glass microsphere optical resonator was proposed and experimentally investigated for chemical vapor sensing. The fiber pigtailed thin wall capillary was proven as an effective coupler for the excitation of WGMs in porous glass microsphere. The ethanol concentration change resulted in the vapor molecule adsorption in the porous channels, which led to the variation of effective refractive index, causing a resonance shift towards longer or shorter wavelength. After calibration, this response can be used for chemical vapor detection. The capillary wall coupled microresonator sensing structure unchains the limitation of optical microresonator in lab use and makes it a reliable lab-in-tube chemical sensing probe in practical applications.

5.4 Optical Resonator Thermal Sensor

5.4.1 Introduction of Optical Thermal Sensors

Another application for thin wall capillary coupled optical resonator is its use in thermal sensing. Accurate temperature monitoring is important in many areas such as environmental control [115], food processing [116] and chemical handling [117]. Optical fiber thermal sensors have a variety of benefits that include lightweight and small size, electromagnetic interference immunity, high sensitivity and possibility of implementing multiplexed or distributed sensor arrays [75]. Various types of optical fiber based temperature sensors were demonstrated including fiber gratings [76, 118, 119], optical interferometers [114, 120] and optical micro resonators [121, 122]. A fiber Bragg grating was reported to have a temperature sensitivity of about 0.013 nm/°C [119] and a long period fiber grating yielded a higher sensitivity of about 0.093 nm/°C [123]. Fiber inline Mach–Zehnder interferometer was shown a thermal response of 0.082 nm/°C [120] and the sensitivity of a femtosecond laser fabricated Michelson interferometer was estimated to be 0.015 nm/°C [114]. Although these grating and interferometer based optical fiber sensors possess high temperature sensitivity, the physical dimensions are typically in the range of millimeter to centimeter, which is excessive for sensing applications in a small volume, such as cell cultures and microfluidics.

On the contrary, WGMs optical microresonators, which are on the scales of micrometers, can be used for temperature measurement in a small volume with high precision [1]. In addition, the temperature sensitivity of microresonators can be further enhanced by the integration with polymer materials, offering one order of magnitude

sensitivity improvement compared with traditional silica glass material based optical fiber sensors [121, 122].

5.4.2 Polymer Microsphere

In this section, a Poly (methyl methacrylate) (PMMA) microsphere coupled by a thin wall capillary was investigated as an optical microresonator for temperature sensing. An optical fiber fusion spliced to a hollow silica capillary tube with a wall thickness of several microns was used to interrogate the PMMA microsphere. The combined thermo-optic and thermo-expansion effects of the PMMA material led to a shift in the resonance wavelength. The thin wall capillary excited PMMA optical microresonator was demonstrated as an alignment-free temperature-sensing probe with a higher sensitivity compared to silica resonator temperature sensors. This miniature sized convenient sensing structure may find broad applications in biomedical applications.

5.4.3 Schematic of PMMA Optical Resonator Thermal Sensor

The thin wall capillary coupled PMMA optical microresonator for temperature sensing is schematically illustrated in Fig. 5.5. The coupler was made by fusion splicing a capillary tube (Polymicro Technologies, LLC, ID/OD 75/150 μm) to a multimode fiber (Corning, 62.5/125). At the joint point, a cone shape was formed. A PMMA microsphere (Cospheric, PMPMS, 65-90 μm) was inserted into the capillary till in contact with the capillary wall at the cone portion. The far end of the capillary was then sealed by arc and

chemically etched using hydrofluoric acid (Acros Organics, 20%) to reduce the wall thickness down to about 2 μm.

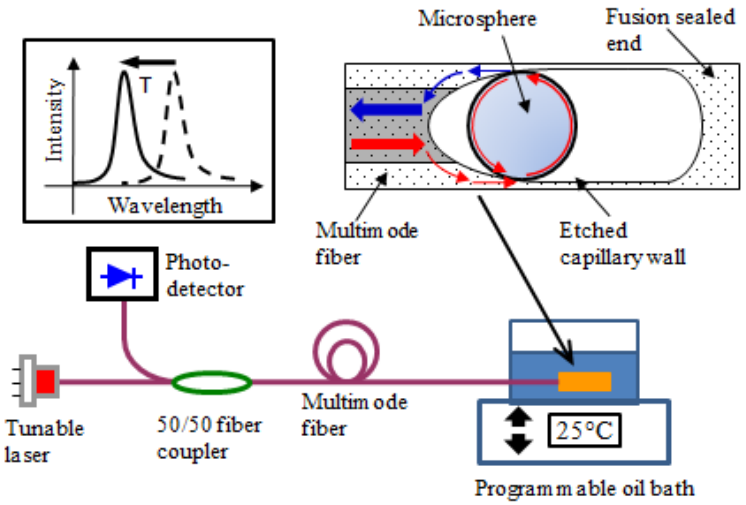

Fig. 5.5. Schematic of thin wall capillary coupled PMMA microresonator for thermal sensing.

5.4.4 Analysis of PMMA Material Thermal Response

The high thermo-optic and thermal expansion coefficients of the PMMA material make it a good candidate for temperature sensing. When the probe was dipped into the water bath (Fisher Scientific Isotemp 205 Digital Waterbath), the PMMA resonator responded to the temperature change to produce a wavelength shift. The thermal response to resonance shift can be modeled using the following equation [121]:

$$\frac{\Delta\lambda}{\Delta T} = \lambda_0 \left(\frac{1}{n}\frac{dn}{dT} + \frac{1}{D}\frac{dD}{dT} \right) \qquad (5.1)$$

where *dn/(dT)*and *dD/dT* are the coefficients of thermo-optic coefficient (TOC) and cofficient of thermalo -expansion (CTE), respectively. λ_0 is the resonance at cold cavity, *D* is the diameter of the microsphere, Δλ and ΔT are the resonance shift and

temperature change of the PMMA microcavitymicroresonator, respectively. The CTE of the PMMA microsphere is 2.02×10^{-4}/°C and the TOC is -1.13×10^{-4}/°C [124]. Compared to silica material, the TOC and CTE of PMMA are three orders and one order higher [122], which proves the capability of higher sensitivity measurement using PMMA microresonator, respectively.

5.4.5 Integration and Cavity Seal

Figure 5.6(a) shows the overview microscopic image of the capillary wall coupled PMMA microsphere resonator sensor, where the PMMA microsphere is in contact with thin wall capillary at the cone region. In Fig. 5.6(a), the yellow light enters the thin wall of at the spliced joint between the fiber and the capillary.

The light is partially coupled into the PMMA microsphere through the evanescent field, shown as the red color circular inside the PMMA microsphere and an optical resonator is thus realized. The WGMs are coupled back and the light propagates backward through the cone shape and detected by the photodetector.

To prevent the contamination, a capillary tube with larger dimension (ID/OD 250/350 μm) protected the whole sensor probe as a sleeve. Fig. 5.6(b) shows the microscopic images of the silica glass microspheres and the PMMA microspheres under the same observation condition.

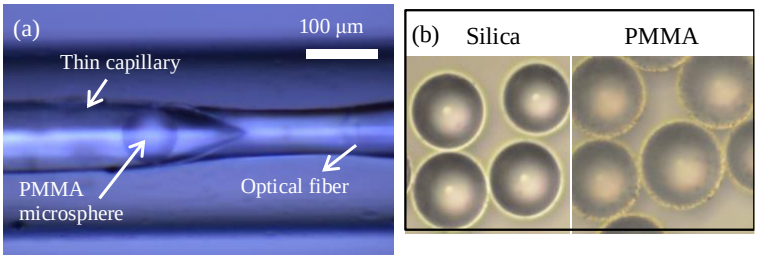

Fig. 5.6. Overview of the capillary wall coupled resonator thermal sensor. (a) The etched capillary integrated with PMMA microsphere; (b) Microscopic images of silica and PMMA spheres under the same observation conditions.

Meanwhile, a sealing process using UV epoxy was also tried instead of using capillary sleeve. When the PMMA microsphere was integrated with the capillary, certain amount of UV adhesive was attached to the open end of the capillary. After UV exposure, the end of the capillary can be firmly sealed, shown as the next figure:

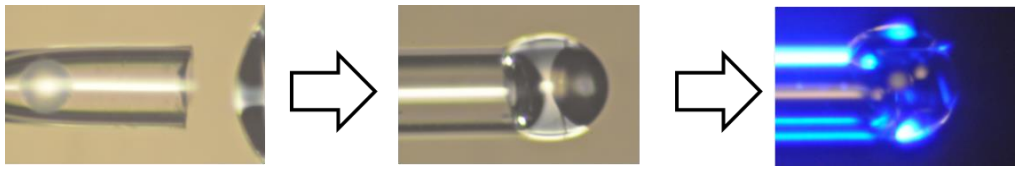

Fig. 5.7. Capillary opening end seal process.

5.4.6 Resonance Spectrum of the PMMA Microsphere Resonator

Figure. 5.8 shows a resonance spectrum of a 85 μm PMMA optical resonator in room temperature. The spectrum shows a clear periodic resonance pattern. The Q-factor was calculated to be 2×10^3 at the resonant wavelength of 1536.37 nm. The corresponding full width at half maximum (FWHM) was 0.76 nm and the free spectrum range (FSR) was 5.93 nm. The mode order numbers are also provided in the figure.

Compared to silica glass microsphere excited by a fiber taper, the Q-factor of capillary wall coupled PMMA sphere resonator was lower. The reasons for low Q-factor

can be attributed to several aspects. The PMMA sphere was in contact with the inner capillary. Thus, the coupling was not at the best coupling position where the excitation waveguide should be at a slight distance (~300 nm) from the resonator [111]. From the material aspect, the silica microspheres had a better transparency while the PMMA beads less transparent due to material nature, as shown in Fig. 5.6 (b), suggesting higher optical loss of the PMMA material. Meanwhile, the PMMA sphere surface roughness might also contributed to a higher scattering loss and lowered the internal Q-factor.

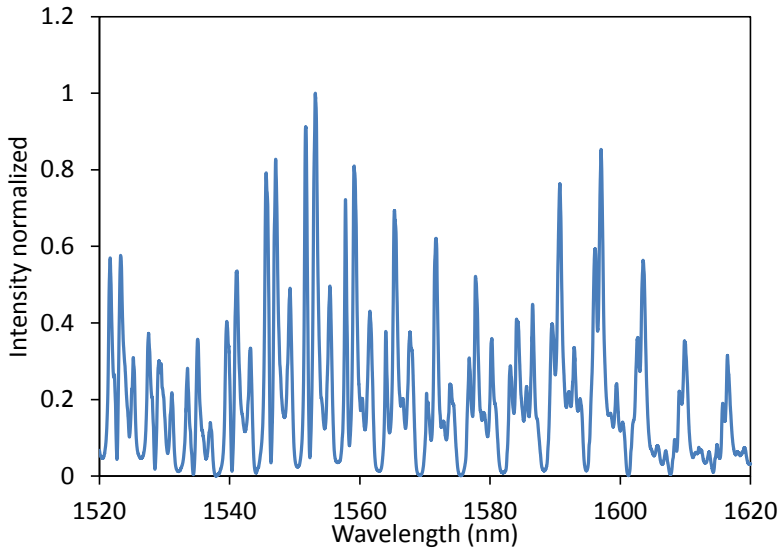

Fig. 5.8. Reflection resonance spectrum of the PMMA resonator coupled by thin wall capillary.

As a comparison, the resonance of the same coupling approach to borosilicate glass microsphere was also tested. The Q was calculated as ~10^4 and higher order modes coupling can be observed. The reflection resonance spectrum signal was acquired when the probe was dipped into DI water. The resonance spectrum is shown in Fig. 5.9.

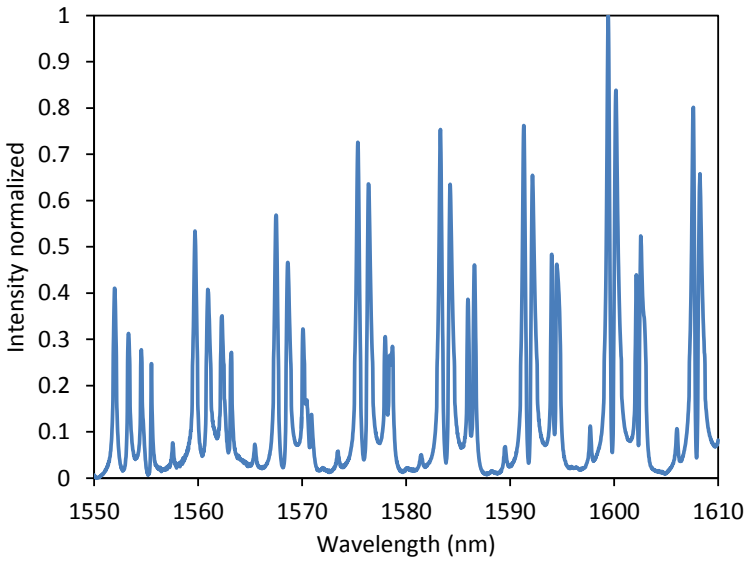

Fig. 5.9. Reflection resonance spectrum of the borosilicate glass microsphere resonator coupled by thin wall capillary in DI water.

Although the Q-factor of the thin wall capillary coupled PMMA microsphere resonator is low, PMMA is more sensitive to temperature variations comparing to silica glass from the material aspect. Meanwhile, the capillary coupler demonstrates a robust excitation approach compared to the fiber taper coupling. As a result, the capillary wall interrogated PMMA microresonators shall have a higher thermal sensitivity and present practical temperature measurement in biomedical applications.

5.4.7 Thermal Sensor Temperature Response

To quantify the temperature measurement, the sensor was then immersed into the bath, as shown in Fig. 5.5. The testing temperature range was set from 28 °C to 36 °C, and the temperature increments were taken stepwisely. The linear relationship between the resonance shift and the temperature change is shown in Fig. 5.10. A total wavelength

shift of 4.5 nm was noticed upon the eight degrees change. Curve-fitting of the resonant peaks was applied to reduce the random intensity noises. The PMMA microsphere resonance thermal response results are shown in Fig. 5.10 (a), which indicates that the increasing temperature leads to a resonance shift towards longer wavelength. Figure 5.10 (b) shows the resonance spectrum of the PMMA resonator and the resonance peak at 1536.31 nm is studied as the target in temperature sensing and the estimated sensitivity is 0.62 nm/°C from the estimate. Based on the measurement, the sensitivity is similar to PDMS coated silica microsphere [122] and one order higher than the silica microsphere and traditional fiber Bragg grating [123]. The difference in experimental result and theoretical estimate is because of the change in microsphere movement due to expansion, so that the coupling condition thus varies.

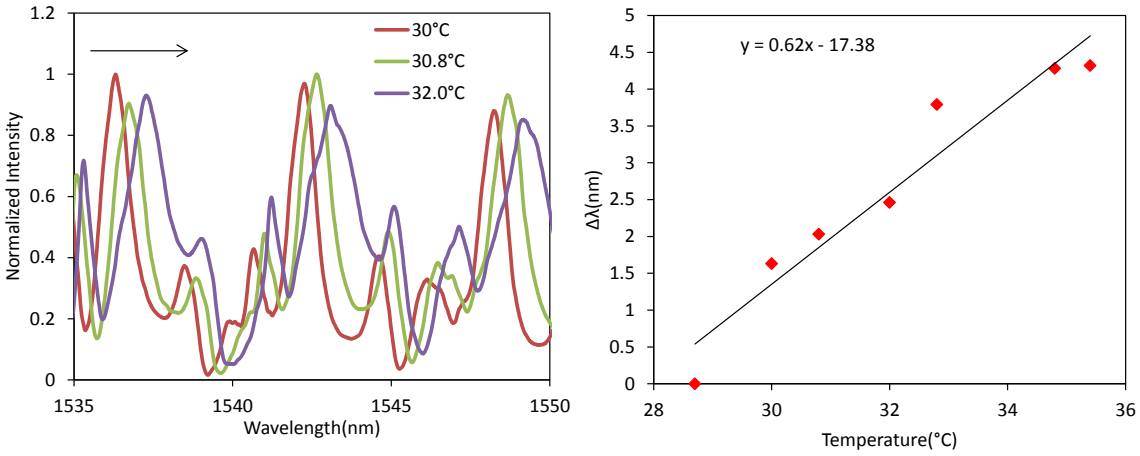

Fig. 5.10. Resonant wavelength shift as a function of temperature increase. Left: Thermal responses of the PMMA optical microresonator sensor at different temperatures, right: linear-fit of the thermal response.

In comparison, the borosilicate sphere integrated thermal probe was also tested, as shown in Fig. 5.11. The testing temperature range was set from 29.9 °C to 38 °C, and the

linear relationship between the resonance shift and the temperature change is shown in the figure. The peak at 1585 nm was monitored for its thermal response. A total wavelength shift of 0.08 nm was noticed upon the eight degrees change. Curve-fitting of the resonant peaks was applied to reduce the random intensity noises. Again, the thermal response trend of the borosilicate glass microsphere indicates that the increasing temperature leads to a resonance shift towards longer wavelength. The estimated sensitivity is 0.01 nm/°C from Fig. 5.11.

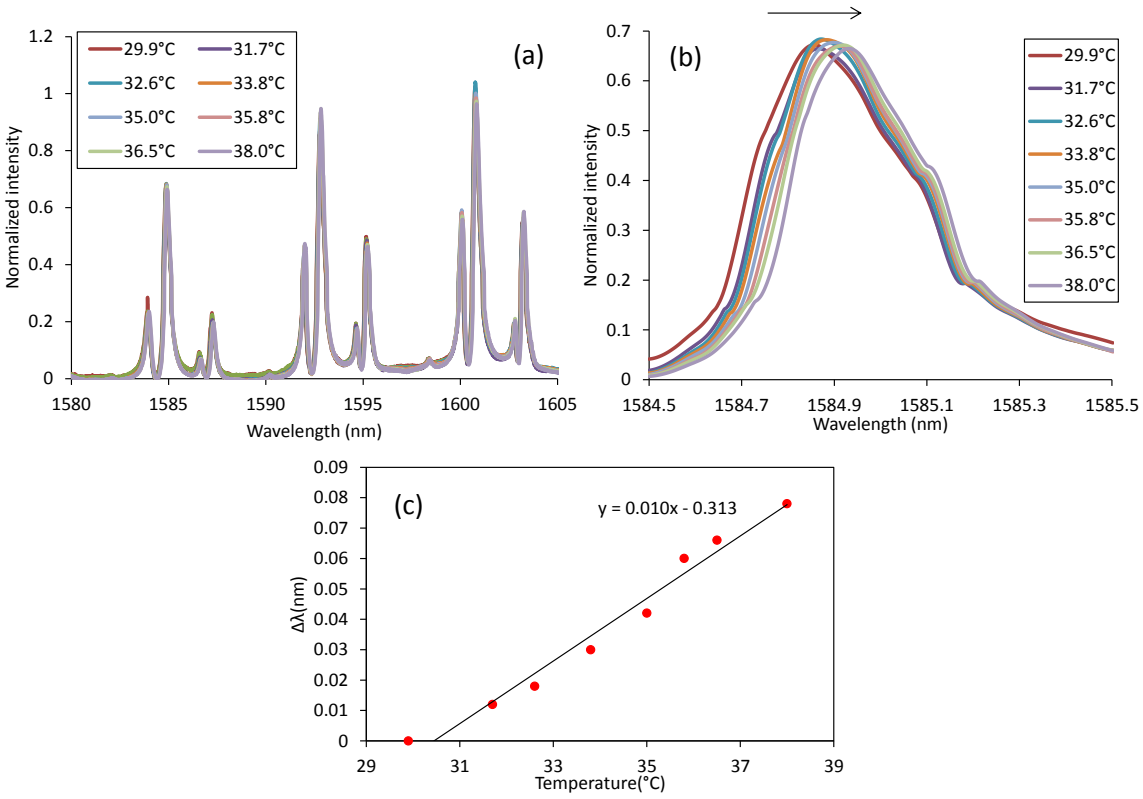

Fig. 5.11. Resonant wavelength shift as a function of temperature increase based on borosilicate microsphere resonator. (a): Thermal responses of the borosilicate optical microresonator sensor at different temperatures, (b): detailed information of the peak at 1585 nm; (c) linear-fit of the thermal response.

In this design, the multipath reflective coupling structure provided an effective excitation of WGMs in multiple dimensions. As a result, the coupling interaction area

between the resonator and the surroundings is enlarged compared to the single dimensional coupling. Also, the fragility nature of fiber taper was improved by using the thin wall capillary as a reliable coupling waveguide, which helped this structure to be a convenient portable sensing probe. Moreover, the sensitivity has been improved by 60 times when polymer sphere was used. This provides a potential for highly sensitive temperature measurement. When combined with a high-resolution detection equipment (0.001 nm per step), then a highly precise measurement can be realized.

In summary, a fiber pigtailed thin wall capillary coupled PMMA microresonator was proposed and experimentally investigated for thermal sensing. The temperature change led to the variation of thermo optic and expansion coefficients in PMMA microsphere, causing a shift in resonance spectrum towards longer or shorter wavelengths. After calibration, this deterministic relation can be used in temperature measurement.

This structure realized a miniaturized temperature sensor probe with high sensitivity compared to silica resonator sensor. Meanwhile, the perturbation of the resonator sensor was improved. This multipath reflective capillary wall structure offered a beneficial coupling platform with higher robustness as well as a convenient portable temperature sensor probe in biomedical applications.

5.5 Refractive Index Measurement

5.5.1 Schematic of Refractive Index Sensor Probe

Refractive index measurement is important in food industries. Precision measurement of index change corresponding to sample concentration variation is crucial for security purpose.

In this section, a sealed cavity with borosilicate glass microsphere was integrated with the thin wall capillary and tested for refractive index sensing. Liquid phase refractive index change was tested with glucose at different concentrations. The schematic of the refractive index sensing is shown in the next figure. When the capillary coupled resonator sensor was dipped into the glucose sample, an increasing concentration of the solution was realized by adding standard sugar into the solution. A constant resonance peak decrease can be noticed thereafter.

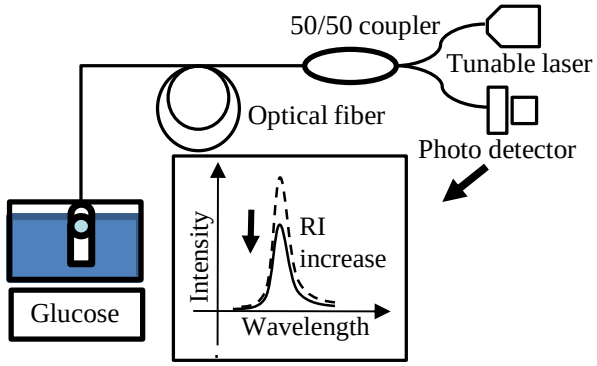

Fig. 5.12. Schematic of thin wall capillary coupled glass microsphere resonator for refractive index sensing.

5.5.2 Resonance Spectra of the Refractive Index Sensor

The resonance spectra in DI water is shown in the next figure as the testing start point. Q factor of 10^5 was noticed at the higher order modes (third outstanding peak in each group). Periodical spectra can be seen in the range of 1520 nm to 1620 nm.

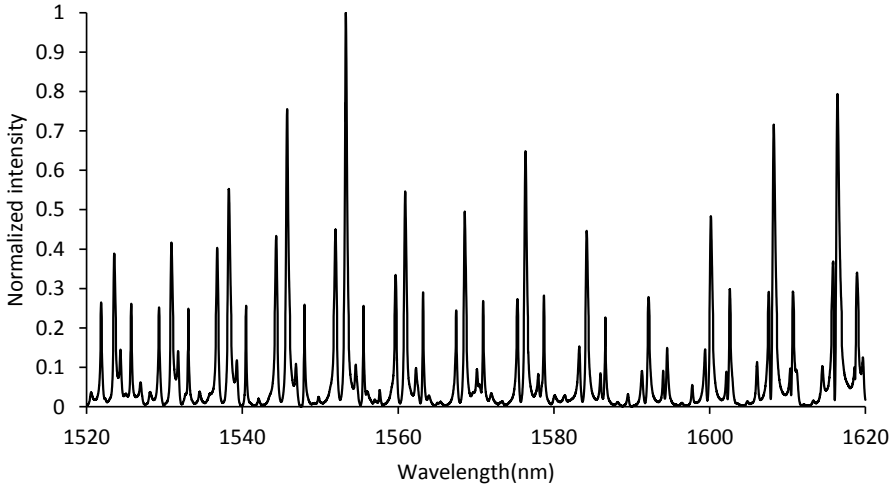

Fig. 5.13. Resonance spectrum of the capillary coupled resonator in DI water.

5.5.3 Refractive Index Measurements

Refractive index ranging from 1.3344 to 1.3847 with fifteen samples was tested with increasing glucose concentrations. The RI change corresponds to the different concentration of the glucose solution. The resonator response to RI change can be seen from Fig. 5.14. The resonance intensity starts to decrease as an increase of refractive index. Different color corresponds to each refractive index value, i.e. glucose concentration. Fifteen refractive index samples were measured. Test stopped at the refractive index value of 1.3847, as the coupling resonance was as low as -60 dBm at the peak intensity.

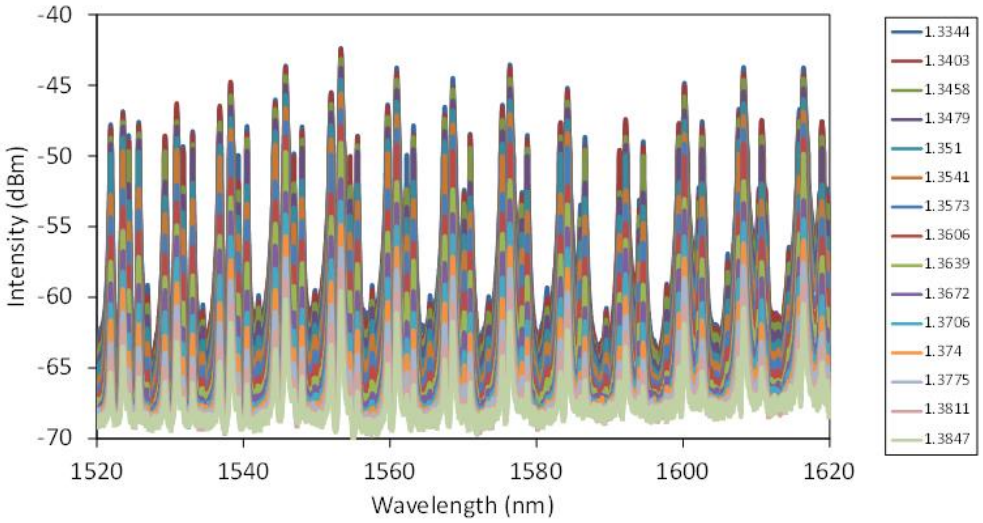

Fig. 5.14. Resonance spectrum response as refractive index increases.

In each resonance peak group, three most significant resonance peaks were analyzed, marked in the labeled dash circles, shown in Fig. 5.13. The reason of choosing this specific resonance group (peak 1: 1553.21 nm, peak 2: 1552.13 and peak 3: 1555.11) is due to the highest visibility throughout the wavelength range.

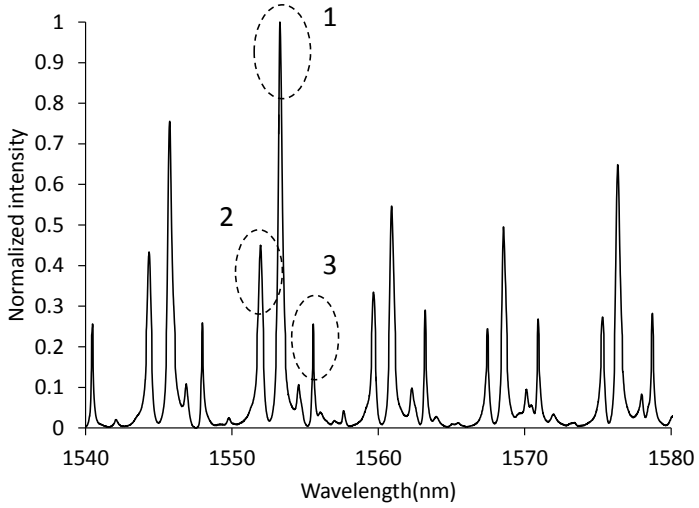

Fig. 5.15. Resonance spectrum peaks of interest.

The relationship of peak intensity as a function of RI responses of the three resonance peaks were analyzed and shown as below.

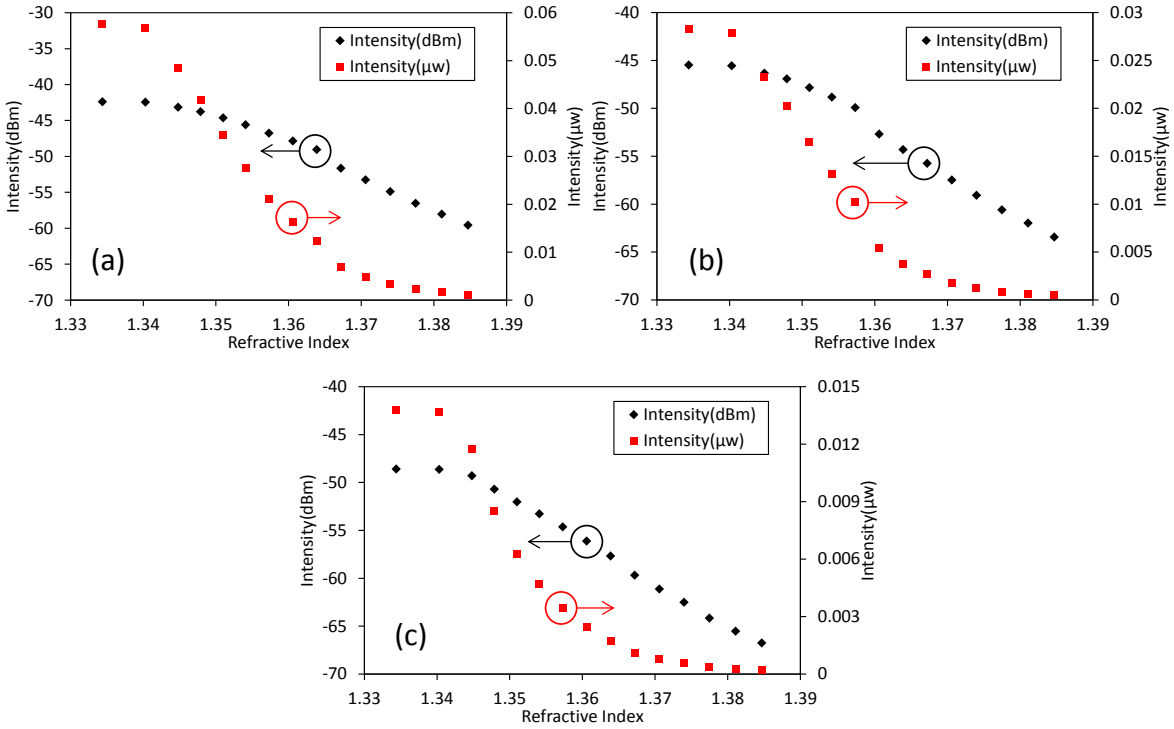

Fig. 5.16. Refractive index measurement. (a) Response of the most significant resonance (b) response of the second most significant resonance (c) response of the third most significant resonance.

Intensity in decibel (black) and standard (red) units were shown in the figure. Linear relationship can be seen in decibel unit in the range of 1.35 to 1.38. In standard unit, the slope exhibits slower trend at the beginning and the end, sharp change exists between 1.34 to 1.365 in the most significant peak, 1.34 to 1.36 in the second most significant peak and 1.345 to 1.355 in the third significant peak; linear relationship can be noticed with these regions.

This indicates the relationship between the resonance and the refractive index change is nonlinear and fundamental mode shows most noticeable response to glucose

concentration variations. The sensitivity as high as 2 μw/RIU can be achieved. This structure realized a miniaturized refractive index sensor probe with high sensitivity. This convenient sensor probe may find broad applications in biomedical applications.

CHAPTER SIX

IONIC LIQUID CORE MICRORING RESONATOR FOR CO_2 DETECTION

6.1 Microring Resonator and the Sensing Applications

In the application of optical microresonators, further benefits can be extended with liquid core involved microring resonators [125]. Biomolecule detection was demonstrated theoretically and experimentally based on liquid core optical ring resonator [126]. Refractometric sensors were presented using two measurement systems with a comparison between optical micro spherical resonator and liquid core ring resonator, and the later presented high sensitivity, stable performance as well as microfluidic compatibility [127]. The core of the ring resonator provides the sensing freedom when chooses for different sensing candidates.

6.2 Ionic Liquid for CO_2 Sequestration

The use of ionic liquid can be seen in a wide range of applications including cellulose dissolution [128], nuclear fuel reprocessing and gas handling [129]. Carbon dioxide absorption by ionic liquid was proven as one of its specialty [130-132]. A task-specific ionic liquid was designed for CO_2 capture by Bates [131], and shown its CO_2 sequestration capability by an observation of the molar ratio between CO_2 and ionic liquid as a function of time; Tang demonstrated the poly(ionic liquid)s as novel polymer materials that selectively absorb CO_2 with higher capacity and faster absorption/desorption rates [132].

6.3 Ionic Liquid Core Microring Resonator

In this chapter, we propose and experimentally demonstrate a CO_2 detector based on an ionic liquid core microring resonator (ILCMRR), for the first time to the best of our knowledge. Because of the ionic liquid sequestration nature on CO_2, the effective refractive index of the ring resonator is changed by CO_2 molecule absorption, which in turn induces a shift in the resonant wavelength of the ionic liquid core ring resonator. Absorption time to equilibrium can be measured by monitoring the wavelength shift.

6.3.1 Fabrication and Principle of ILCMRR

The experimental setup is shown in Fig. 6.1. A fiber taper with a length of ~1 cm and a diameter of ~ 2 μm was fabricated from the standard single mode fiber (Corning SMF-28) using a fiber tapering system. A 50 μm diameter capillary with wall thickness of 1 μm was filled with ionic liquid. The ionic liquid core capillary was placed in contact with the optical fiber taper using a precision micro positioning system. When light from a tunable laser source (HP-8168F) passed through the taper, part of it will be coupled in to the ionic liquid core capillary; then the Whispering Gallery Modes (WGMs) ILCMRR were formed. When the ILCMRR was placed in a chamber and immersed with CO_2 gas, the chemical molecules absorbed by the ionic core of the ILCMRR led to certain refractive index change. Thus, a relative resonance shift can be observed by a programmable controlled optical spectrum analyzer (Ando AQ6319).

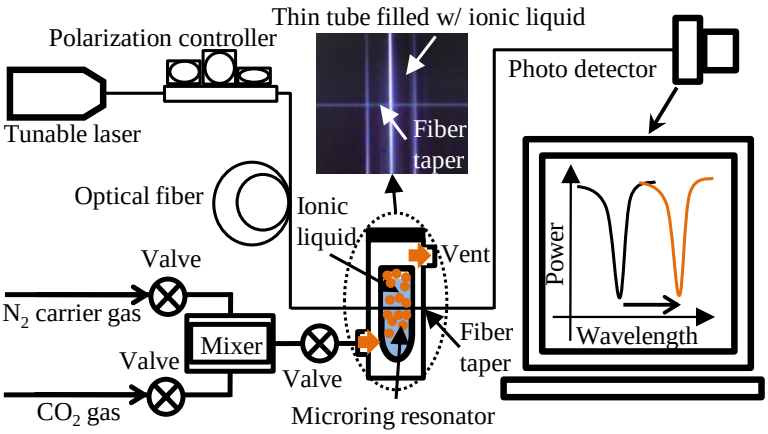

Fig. 6.1. Schematic of ionic liquid core microring resonator for CO_2 detection.

6.3.2 Microring Resonator Responses to CO_2 gas

Before filling the core with ionic liquid, the thin capillary ring resonator transmission spectrum and its response to CO_2 are shown in Fig. 6.2. In the experiment, the inner diameter of the thin wall capillary was 50 μm. The fiber taper was perpendicularly coupled to the thin wall (~1 μm) capillary, measured by a measuring optical microscope (Nikon MC-203). The cone shape was created by fusion splicing the capillary with a section of the optical fiber, which served as the ILCMRR sensor holder. When the hollow capillary ring resonator was tested for its CO_2 response, a relative resonance wavelength shift of 0.02 nm was noticed. The corresponding mode order numbers are provided in Fig. 6.2.

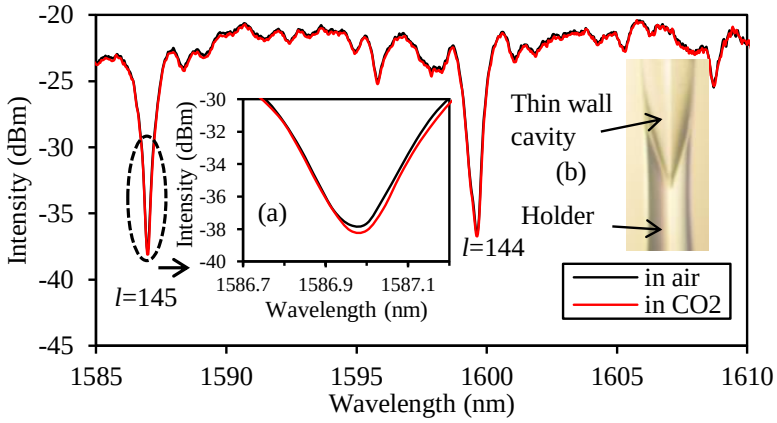

Fig. 6.2. (a) Transmission resonance spectrum of the hollow thin capillary microring resonator and its response to CO2. Insets: (a) the resonance shift in details at the dip highlighted and (b) the overview of the cavity with the fiber holder.

6.3.3 Transmission Resonance of ILCMRR

When the capillary was filled with ionic liquid, the resonance spectrum of the ILCMRR was shown as Fig. 6.3. In the experiment, the estimated quality factor of the ILCMRR was ~1000. The resonance efficiency was decreased due to the following reasons: first, the increase of core refractive index led to higher light adsorption; second, the impurity of the ionic liquid core introduced higher scattering loss. The ionic liquid employed in this study is a product of Sigma-Aldrich Company. The ionic liquid sample is composed of Hexyl-methylimidazolium bisimide.

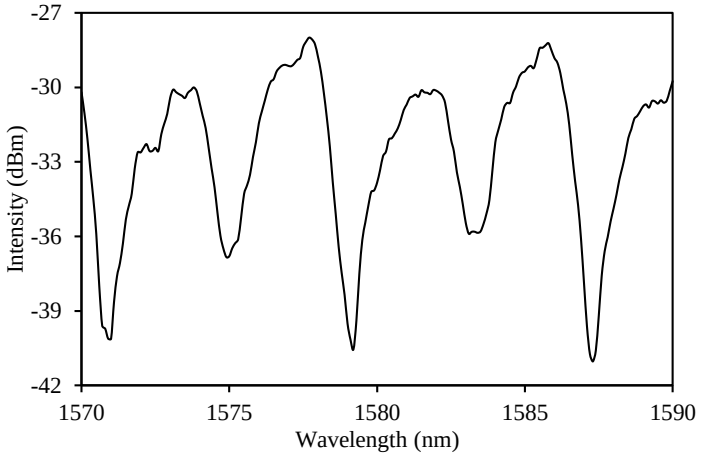

Fig. 6.3. Transmission resonance spectrum of the ILCMRR.

6.3.4 ILCMRR CO_2 Sensing and Time Response

ILCMRR to CO_2 sequestration time response was measured. The test was carried out in the following steps as shown in Fig. 6.1: first, the one micron thin wall capillary filled with ionic liquid was perpendicularly coupled to fiber taper and positioned inside a chamber; second, the chamber was inflated with nitrogen carrier gas; third, the valve of CO_2 gas was turned on and CO_2 started to flow into the chamber; fourth, programmable photo detector recorded resonance spectrum and the measurement was started when CO_2 gas was filled with the chamber. A total measurement time of 300 seconds was tested and an equilibrium state of absorption was attained.

Figure 6.4 shows the time responses of the transmission spectra of the ILCMRR in CO_2 absorption. The response in Fig. 6.4 indicates that the ILCMRR absorption of CO_2 results in a corresponding resonance shift toward longer wavelength. The variation of the resonance spectrum shape was noticed, indicating the change of coupling condition during the CO_2 sequestration process. The coupling efficiency at fundamental mode was

decreased noted by the reduction of the resonance fringe visibility. This was caused by the effective refractive index increase during the CO_2 absorption. A third-order Savitzky–Golay filter was applied to the original spectra to eliminate the random high frequency intensity noise and spectral ripples. The location of the resonance dip was not changed by the smoothing approach, which can be verified by the comparison of original and smoothed 0 second resonance spectrum as shown in Fig. 6.4.

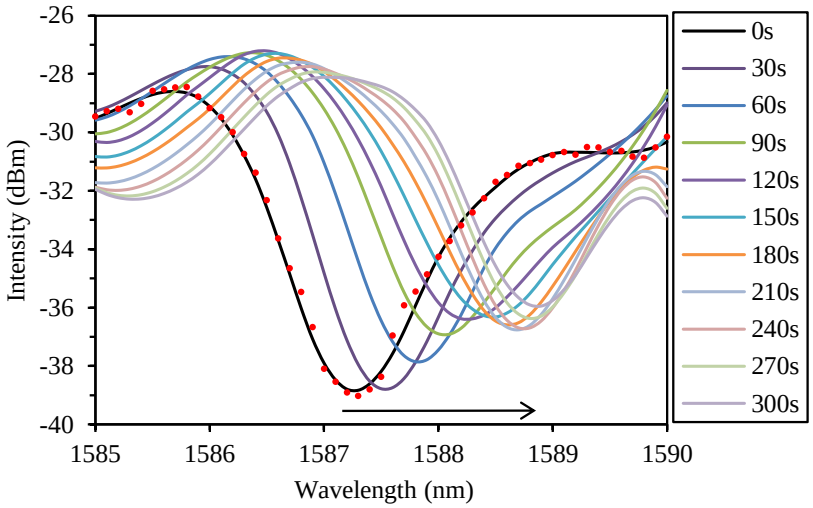

Fig. 6.4. ILCMRR time response to CO2 absorption. Curve fitting of the 0 second response was provided.

The time to equilibrium curve was shown in Fig. 6.5 with a total resonance spectra shift of 1.55 nm. A linear response was witnessed at the first 80 seconds of testing, shown as the range in the red dashed region with the detailed measurement in the inset of Fig. 6.5. A slower CO_2 sequestration pace indicated that the saturation status of the ionic liquid was achieved after 210 seconds of absorption. No obvious resonance spectra shift can be seen after 240 seconds of testing. The polynomial fitting equations and the correlation were given in Fig. 6.5.

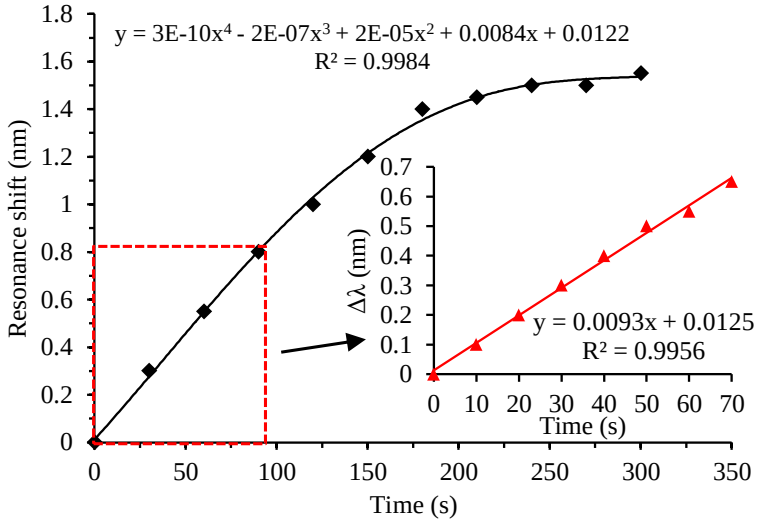

Fig. 6.5. Time to equilibrium curve of ILCMRR on CO_2 sequestration. Inset: linear time response at initial CO_2 detection.

In summary, an original ionic liquid core microring resonator was proposed and experimentally investigated for CO_2 detection. The CO_2 absorbed by the ionic liquid core led to an effective refractive index change. The one-micron thin capillary wall offered good interaction between the absorption and the resonance circulating along the capillary surface, causing a shift in resonance wavelength towards a longer wavelength. The ILCMRR provides a beneficial platform for CO_2 detection and leads to a broad chemical sensing applications.

CHAPTER SEVEN

CONCLUSION AND FUTURE WORK

7.1 CONCLUSIONS

In this dissertation, the optical microresonator was demonstrated for sensing applications. Microsphere and microring resonators were investigated in this work. The quality of the optical microresonator with high-Q, miniature size and high detection sensitivity make it a good candidate for chemical detection, thermal sensing, refractive index measurement, etc.

In order to enhance the sensitivity, certain structures and materials were utilized. Porous glass microsphere was used to fully extend the molecule adsorption and a remarkable effective refractive index change was presented thereafter. The resonance wavelength shift was thus noticed and recorded as the measurement of environmental chemical vapor change. Modeling and simulations were studied for a comprehensive understanding of the sensing application as a function of porous shell thickness and electric and magnetic mode dependency.

In thermal sensing, polymer material was tested with higher thermal responses. High sensitivity temperature measurement was realized using the capillary wall coupled PMMA resonator probe.

Liquid phase refractive index measurement was realized by measuring the coupling efficiency change as a function of glucose concentration variations, which may find broad applications in food industry and biosensing areas. Additionally, ionic liquid core resonator was demonstrated as a gas detector due to its selective sequestration on

CO_2. This structure provides an ideal candidate for gas monitoring and control in chemical engineering.

A novel fiber pigtailed thin wall capillary coupler was designed. This new coupler demonstrated efficient excitation of WGMs resonator when integrated with microspheres. Traditional coupler with disadvantages of fragility, bulkiness and precision fabrication were overcome. This provides the potential for the development of convenient optical resonator sensor probes based on the reflective coupling.

7.2 FUTURE WORK

Broad applications on optical sensors will be investigated based on the thin wall coupled microresonator structure. Analytical study and comprehensive understanding of the coupling scheme will be investigated.

1. Capillary wall coupled optical resonator acoustic sensor probe. Microsphere sphere material with higher acoustic wave responses will be investigated. A highly sensitive acoustic probe may find broad applications in ocean optics, geometry monitoring, etc.
2. Distributed sensing applications will be investigated. Multiple microspheres with different materials and structures will be helpful for distributed sensing applications for different locations or sensing targets.
3. Miniaturized micro-gyroscope will be studied. The multiple coupling optical paths provide the possibility of path mismatches when the microsphere swings in different directions.

4. Cancer cell detection and separation in bio-sensing area will be studied. Thermal sensor probe in cell temperature measurement, microring resonator as cell counter or monitor will be analyzed. The potential uses can be in human health, biomedical areas.
5. Rare earth doped (Erbium, Ytterbium) glass microsphere can be a good candidate for microcavity lasing applications. Various pump approaches were discussed for efficiency pumping of microcavity lasers [78]. The concentration of the doping rate can be tuned at different combinations. A co-doped borosilicate glass sphere was inserted into the etched capillary of inner diameter 100μm, and then a fiber taper was inserted for the purpose of side pumping the microsphere. The dimension of the fiber tip was about 20 μm, shown as Fig. 7.1:

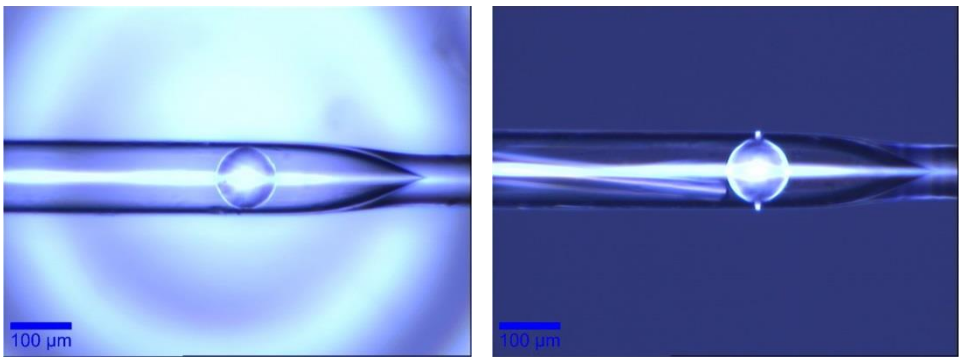

Fig. 7.1. Overview of capillary integrated codoped microsphere and fiber taper side pump.

Once the pump started to increase, the microsphere shown green luminance, although they were not in a circular shape, and shown as:

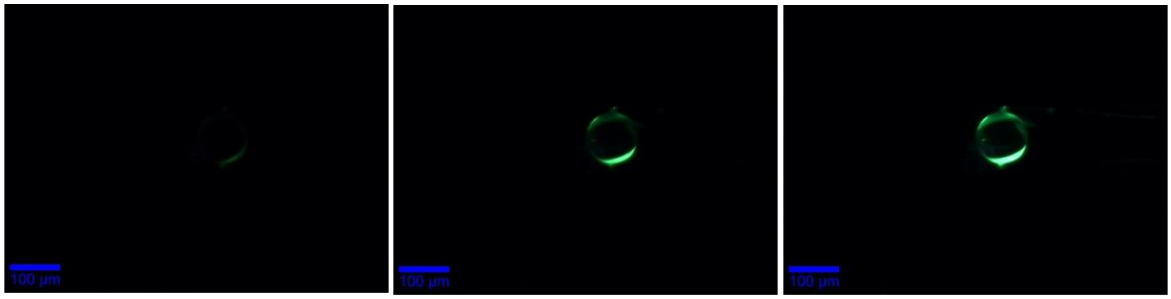

Fig. 7.2. Green laser intensity as an increase of pump source.

Investigation of the lasing parameters (threshold, laser wavelength, etc.) will be discussed in future works.

APPENDICES

Appendix A

Fiber taper fabrication and PWHGM fixation process

The approaches of fiber tapering were realized by the following devices: bidirectional motion stage, linear actuator, LabVIEW programming motion control and CCD-LCD monitoring.

Hydro-oxygen flame and propane flame heat treatment were both tried to optimize the optical fiber taper quality in thickness and transmission loss. After certain combination of tapering duration, velocity and heating strength, a fiber taper of one μm in diameter and less than 0.5 dB transmission losses can be obtained.

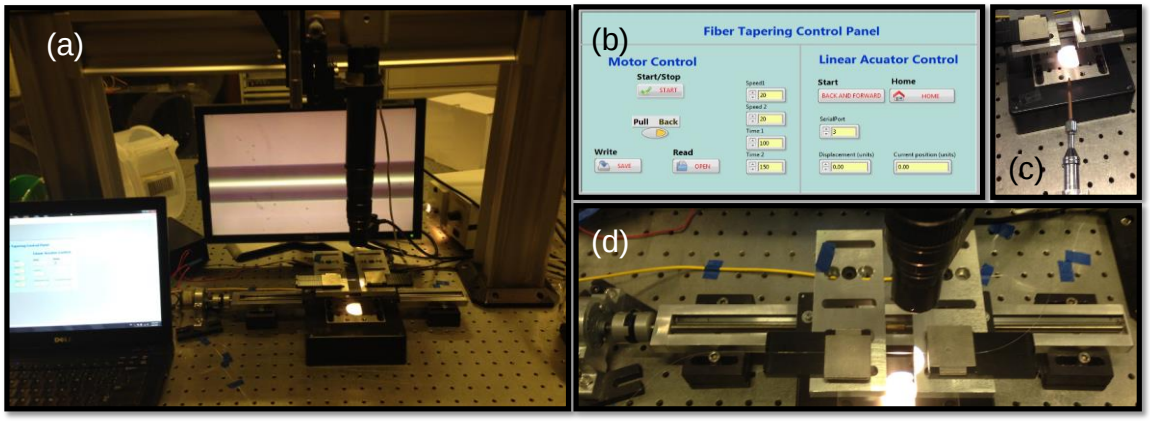

Fig. A.1. (a) Overview of the fiber tapering system; (b) LabVIEW programming control panel; (c) flame torch with linear actuator control; (d) bidirectional stretching system.

In order to realize the side coupling of the PWHGM to fiber taper, the fixation process of PWHGM was carried out as following: 1. The fiber holder was filmed with thin ultraviolet (UV) epoxy; 2. One PWHGM was in contact with the end of the fiber holder; 3. UV light was exposed to the PWHGM to solidity the joint area. UV epoxy was

picked by very little amount: little volume of epoxy was sandwiched by two glass slides, and then the tapered fiber end was slightly in contacted and grab a bit adhesive from the thin epoxy film.

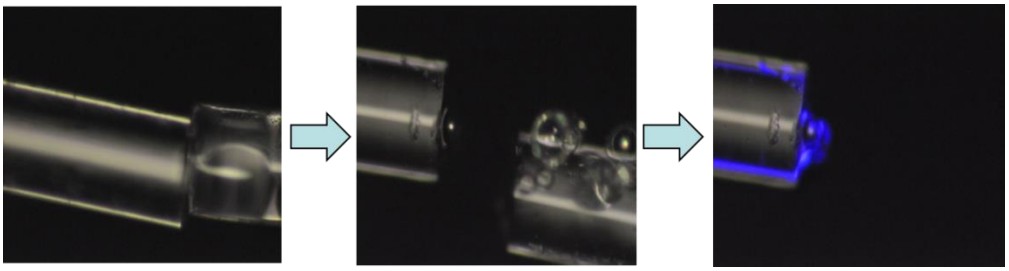

Fig. A.2. PWHGM fixation process. Epoxy attached PWHGM was fixed by UV exposure.

Appendix B

Manufacture of fiber pigtailed thin wall coupler and its integration with microsphere

Fiber pigtailed thin wall coupler was fabricated based on the following process: 1. Multimode fiber (ID/OD:62.5/125) was cleaved with a smooth endface; 2. Fused silica capillary tube was cleaved and smooth ring shape endface was ensured; 3. Sumitomo T-36 fusion splicer was used and the two cleaved ends of MMF and capillary tube were aligned end to end, slight mismatch was due to the dimension differences, as shown in the next figure:

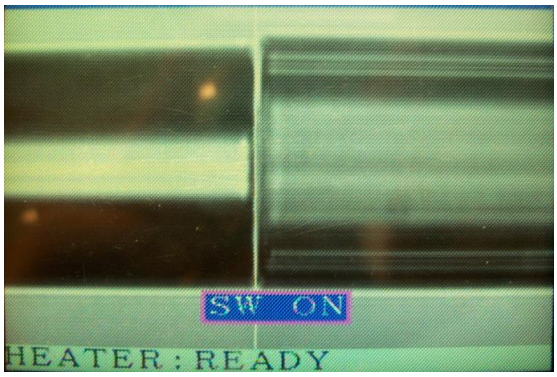

Fig. B.1. MMF and capillary tube alignment under the view of fusion splicer monitor. Left: MMF, right: capillary tube.

4. Fusion splicing option was selected as the standard multimode fiber operation. After the splicing process, a cone shape joint was given as:

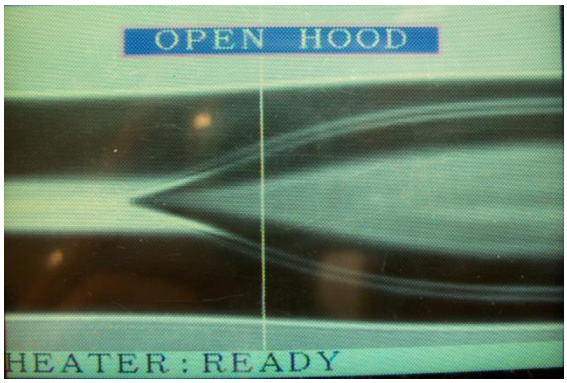

Fig. B.2. fiber pigtailed capillary coupler after fusion splicing.

5. Microsphere was gently inserted into the other end of the capillary end. A section of fiber taper was used to assist the integration process.

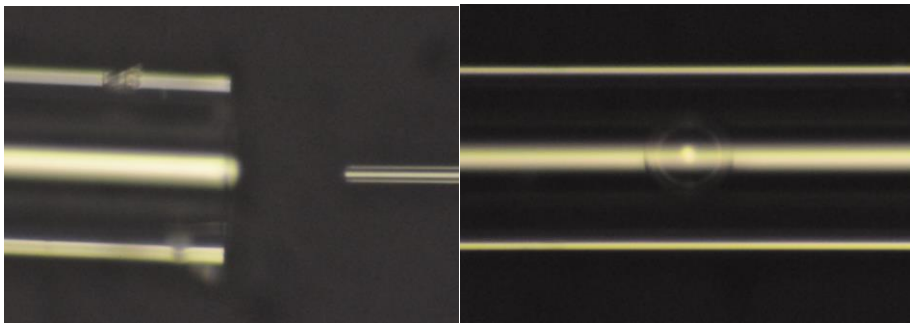

Fig. B.3. Insertion of microsphere into the capillary. Left: fiber taper tip was used as a pushing tool; right: microsphere inserted into the capillary.

6. When the microsphere was inserted into the cone shape area with no more space to move forward; then the other end of the capillary opening was sealed by a section of optical fiber. Minimum fusion splicing was used so that the microsphere was not melted during the sealing process. The details of the fusion splicing information were given as ARC DURATION: 01.00, PREFUSION: 00.10, ARC GAP: 10.00, OVERLAP: 07.00, ARC POWER: 0009.

7. Once the cavity was sealed with microsphere, an etching process was taken using 45% (beginning) - 20% (later) concentration hydrofluoric acid solutions. The etching was stopped when the wall of the capillary was as thin as several microns with good resonance spectrum.

REFERENCE

[1] A. B. Matsko and V. S. Ilchenko, "Optical resonators with whispering-gallery modes - Part I: Basics," *IEEE Journal on Selected Topics in Quantum Electronics,* vol. 12, pp. 3-14, 2006.

[2] T. M. Benson, S. V. Boriskina, P. Sewell, A. Vukovic, A. I. Nosich, V. Janyani, *et al.*, "Micro-resonators: Simulation and application," 2005, pp. 6-11.

[3] F. Vollmer and S. Arnold, "Whispering-gallery-mode biosensing: Label-free detection down to single molecules," *Nature Methods,* vol. 5, pp. 591-596, 2008.

[4] N. M. Hanumegowda, I. M. White, and X. Fan, "Aqueous mercuric ion detection with microsphere optical ring resonator sensors," *Sensors and Actuators, B: Chemical,* vol. 120, pp. 207-212, 2006.

[5] J. C. Knight, G. Cheung, F. Jacques, and T. A. Birks, "Phase-matched excitation of whispering-gallery-mode resonances by a fiber taper," *Optics Letters,* vol. 22, pp. 1129-1131, 1997/08/01 1997.

[6] J. G. Zhu, S. K. Ozdemir, Y. F. Xiao, L. Li, L. N. He, D. R. Chen, *et al.*, "On-chip single nanoparticle detection and sizing by mode splitting in an ultrahigh-Q microresonator," *Nature Photonics,* vol. 4, pp. 46-49, Jan 2010.

[7] J. C. Galas, J. Torres, M. Belotti, Q. Kou, and Y. Chen, "Microfluidic tunable dye laser with integrated mixer and ring resonator," *Applied Physics Letters,* vol. 86, pp. -, 2005.

[8] S. I. Shopova, H. Zhou, X. Fan, and P. Zhang, "Optofluidic ring resonator based dye laser," *Applied Physics Letters,* vol. 90, pp. -, 2007.

[9] C. F. Carlborg, K. B. Gylfason, A. Kazmierczak, F. Dortu, M. J. B. Polo, A. M. Catala, *et al.*, "A packaged optical slot-waveguide ring resonator sensor array for multiplex label-free assays in labs-on-chips," *Lab on a Chip,* vol. 10, pp. 281-290, 2010.

[10] A. H. J. Yang and D. Erickson, "Optofluidic ring resonator switch for optical particle transport," *Lab on a Chip,* vol. 10, pp. 769-774, 2010.

[11] A. Francois, K. J. Rowland, and T. M. Monro, "Highly efficient excitation and detection of whispering gallery modes in a dye-doped microsphere using a microstructured optical fiber," *Applied Physics Letters,* vol. 99, Oct 2011.

[12] A. Francois, K. J. Rowland, V. S. Afshar, M. R. Henderson, and T. M. Monro, "Enhancing the radiation efficiency of dye doped whispering gallery mode microresonators," *Optics Express,* vol. 21, pp. 22566-22577, Sep 2013.

[13] X. S. Jiang, L. M. Tong, G. Vienne, X. Guo, A. Tsao, Q. Yang, *et al.*, "Demonstration of optical microfiber knot resonators," *Applied Physics Letters,* vol. 88, May 2006.

[14] K. Takazawa, J. Inoue, and K. Mitsuishi, "Optical Microring Resonators Constructed from Organic Dye Nanofibers and Their Application to Miniaturized Channel Drop/Add Filters," *Acs Applied Materials & Interfaces,* vol. 5, pp. 6182-6188, Jul 2013.

[15] B. E. Little, S. T. Chu, H. A. Haus, J. Foresi, and J. P. Laine, "Microring resonator channel dropping filters," *Lightwave Technology, Journal of,* vol. 15, pp. 998-1005, 1997.

[16] B. E. Little, J. S. Foresi, G. Steinmeyer, E. R. Thoen, S. T. Chu, H. A. Haus, *et al.*, "Ultra-compact Si-SiO₂ microring resonator optical channel dropping filters," *Photonics Technology Letters, IEEE,* vol. 10, pp. 549-551, 1998.

[17] B. E. Little, S. T. Chu, P. P. Absil, J. V. Hryniewicz, F. G. Johnson, F. Seiferth, *et al.*, "Very high-order microring resonator filters for WDM applications," *Photonics Technology Letters, IEEE,* vol. 16, pp. 2263-2265, 2004.

[18] L. Zhou and A. W. Poon, "Electrically reconfigurable silicon microring resonator-based filter with waveguide-coupled feedback," *Optics Express,* vol. 15, pp. 9194-9204, 2007/07/23 2007.

[19] S. M. Spillane, T. J. Kippenberg, K. J. Vahala, K. W. Goh, E. Wilcut, and H. J. Kimble, "Ultrahigh-Q toroidal microresonators for cavity quantum electrodynamics," *Physical Review A,* vol. 71, Jan 2005.

[20] D. K. Armani, T. J. Kippenberg, S. M. Spillane, and K. J. Vahala, "Ultra-high-Q toroid microcavity on a chip," *Nature,* vol. 421, pp. 925-928, Feb 2003.

[21] J. Ye, D. Vernooy, and H. Kimble, "Trapping of single atoms in cavity QED," *Physical Review Letters,* vol. 83, p. 4987, 1999.

[22] S. M. Spillane, T. J. Kippenberg, O. J. Painter, and K. J. Vahala, "Ideality in a Fiber-Taper-Coupled Microresonator System for Application to Cavity Quantum Electrodynamics," *Physical Review Letters,* vol. 91, p. 043902, 07/22/ 2003.

[23] Y. Louyer, D. Meschede, and A. Rauschenbeutel, "Tunable whispering-gallery-mode resonators for cavity quantum electrodynamics," *Physical Review A,* vol. 72, p. 031801, 09/15/ 2005.

[24] S. L. McCall, A. F. J. Levi, R. E. Slusher, S. J. Pearton, and R. A. Logan, "Whispering‐gallery mode microdisk lasers," *Applied Physics Letters,* vol. 60, pp. 289-291, 1992.

[25] S. Spillane, T. Kippenberg, and K. Vahala, "Ultralow-threshold Raman laser using a spherical dielectric microcavity," *Nature,* vol. 415, pp. 621-623, 2002.

[26] H.-B. Lin and A. Campillo, "CW nonlinear optics in droplet microcavities displaying enhanced gain," *Physical review letters,* vol. 73, p. 2440, 1994.

[27] L. Yang and K. Vahala, "Gain functionalization of silica microresonators," *Optics letters,* vol. 28, pp. 592-594, 2003.

[28] L. Yang, T. Carmon, B. Min, S. M. Spillane, and K. J. Vahala, "Erbium-doped and Raman microlasers on a silicon chip fabricated by the sol–gel process," *Applied Physics Letters,* vol. 86, pp. 091114-091114-3, 2005.

[29] P. Del'Haye, A. Schliesser, O. Arcizet, T. Wilken, R. Holzwarth, and T. Kippenberg, "Optical frequency comb generation from a monolithic microresonator," *Nature,* vol. 450, pp. 1214-1217, 2007.

[30] T. Kippenberg, R. Holzwarth, and S. Diddams, "Microresonator-based optical frequency combs," *Science,* vol. 332, pp. 555-559, 2011.

[31] V. S. Ilchenko, A. A. Savchenkov, A. B. Matsko, and L. Maleki, "Nonlinear optics and crystalline whispering gallery mode cavities," *Physical review letters,* vol. 92, p. 043903, 2004.

[32] A. B. Matsko, A. A. Savchenkov, D. Strekalov, V. S. Ilchenko, and L. Maleki, "Optical hyperparametric oscillations in a whispering-gallery-mode resonator: Threshold and phase diffusion," *Physical Review A,* vol. 71, p. 033804, 2005.

[33] J. Fürst, D. Strekalov, D. Elser, M. Lassen, U. L. Andersen, C. Marquardt, *et al.*, "Naturally phase-matched second-harmonic generation in a whispering-gallery-mode resonator," *Physical review letters,* vol. 104, p. 153901, 2010.

[34] K. Grattan and T. Sun, "Fiber optic sensor technology: an overview," *Sensors and Actuators A: Physical,* vol. 82, pp. 40-61, 2000.

[35] K. T. Grattan and B. Meggitt, *Optical fiber sensor technology* vol. 1: Springer, 1995.

[36] X. Fan, I. M. White, S. I. Shopova, H. Zhu, J. D. Suter, and Y. Sun, "Sensitive optical biosensors for unlabeled targets: A review," *analytica chimica acta,* vol. 620, pp. 8-26, 2008.

[37] H. Xiao, J. Deng, G. Pickrell, R. G. May, and A. Wang, "Single-crystal sapphire fiber-based strain sensor for high-temperature applications," *Journal of lightwave technology,* vol. 21, p. 2276, 2003.

[38] P. S. Tubel, "Method and system for monitoring smart structures utilizing distributed optical sensors," ed: Google Patents, 2005.

[39] H. Xiao, J. Deng, Z. Wang, W. Huo, P. Zhang, M. Luo, *et al.*, "Fiber optic pressure sensor with self-compensation capability for harsh environment applications," *Optical Engineering,* vol. 44, pp. 054403-054403-10, 2005.

[40] Q. Yu and X. Zhou, "Pressure sensor based on the fiber-optic extrinsic Fabry-Perot interferometer," *Photonic Sensors,* vol. 1, pp. 72-83, 2011.

[41] J. Huang, X. Lan, H. Wang, L. Yuan, T. Wei, Z. Gao, *et al.*, "Polymer optical fiber for large strain measurement based on multimode interference," *Optics letters,* vol. 37, pp. 4308-4310, 2012.

[42] C. von Bültzingslöwen, A. K. McEvoy, C. McDonagh, B. D. MacCraith, I. Klimant, C. Krause, *et al.*, "Sol–gel based optical carbon dioxide sensor employing dual luminophore referencing for application in food packaging technology," *Analyst,* vol. 127, pp. 1478-1483, 2002.

[43] M. Bener, M. Özyürek, K. Güçlü, and R. a. Apak, "Development of a Low-cost optical sensor for cupric reducing antioxidant capacity measurement of food extracts," *Analytical chemistry,* vol. 82, pp. 4252-4258, 2010.

[44] X. Lan, Q. Han, T. Wei, J. Huang, and H. Xiao, "Turn-around-point long-period fiber gratings fabricated by CO laser point-by-point irradiations," *Photonics Technology Letters, IEEE,* vol. 23, pp. 1664-1666, 2011.

[45] T. A. Dickinson, J. White, J. S. Kauer, and D. R. Walt, "A chemical-detecting system based on a cross-reactive optical sensor array," *Nature,* vol. 382, pp. 697-700, 1996.

[46] K. Matsubara, S. Kawata, and S. Minami, "Optical chemical sensor based on surface plasmon measurement," *Applied Optics,* vol. 27, pp. 1160-1163, 1988.

[47] X.-B. Zhang, C.-C. Guo, Z.-Z. Li, G.-L. Shen, and R.-Q. Yu, "An optical fiber chemical sensor for mercury ions based on a porphyrin dimer," *Analytical chemistry,* vol. 74, pp. 821-825, 2002.

[48] X. Lan, B. Cheng, Q. Yang, J. Huang, H. Wang, Y. Ma, *et al.*, "Reflection based extraordinary optical transmission fiber optic probe for refractive index sensing," *Sensors and Actuators B: Chemical,* vol. 193, pp. 95-99, 2014.

[49] J. Huang, X. Lan, A. Kaur, H. Wang, L. Yuan, and H. Xiao, "Temperature compensated refractometer based on a cascaded SMS/LPFG fiber structure," *Sensors and Actuators B: Chemical,* vol. 198, pp. 384-387, 2014.

[50] J. Huang, X. Lan, A. Kaur, H. Wang, L. Yuan, and H. Xiao, "Reflection-based phase-shifted long period fiber grating for simultaneous measurement of temperature and refractive index," *Optical Engineering,* vol. 52, pp. 014404-014404, 2013.

[51] J. Dakin, D. Pratt, G. Bibby, and J. Ross, "Distributed optical fibre Raman temperature sensor using a semiconductor light source and detector," *Electronics Letters,* vol. 21, pp. 569-570, 1985.

[52] J. R. Dunphy, P. Ferraro, S. I. Imparato, G. Meltz, M. Signorazzi, A. Vannucci, *et al.*, "Embedded optical sensor capable of strain and temperature measurement using a single diffraction grating," ed: Google Patents, 1995.

[53] M. Farries, M. Fermann, R. Laming, S. Poole, D. Payne, and A. Leach, "Distributed temperature sensor using Nd3+-doped optical fibre," *Electronics Letters,* vol. 22, pp. 418-419, 1986.

[54] R. Cush, J. Cronin, W. Stewart, C. Maule, J. Molloy, and N. Goddard, "The resonant mirror: a novel optical biosensor for direct sensing of biomolecular interactions Part I: Principle of operation and associated instrumentation," *Biosensors and Bioelectronics,* vol. 8, pp. 347-354, 1993.

[55] A. J. Haes and R. P. Van Duyne, "A nanoscale optical biosensor: sensitivity and selectivity of an approach based on the localized surface plasmon resonance spectroscopy of triangular silver nanoparticles," *Journal of the American Chemical Society,* vol. 124, pp. 10596-10604, 2002.

[56] A. J. Haes, L. Chang, W. L. Klein, and R. P. Van Duyne, "Detection of a biomarker for Alzheimer's disease from synthetic and clinical samples using a nanoscale optical biosensor," *Journal of the American Chemical Society,* vol. 127, pp. 2264-2271, 2005.

[57] K.-P. S. Dancil, D. P. Greiner, and M. J. Sailor, "A porous silicon optical biosensor: detection of reversible binding of IgG to a protein A-modified surface," *Journal of the American Chemical Society,* vol. 121, pp. 7925-7930, 1999.

[58] A. D. Kersey, M. A. Davis, H. J. Patrick, M. LeBlanc, K. Koo, C. Askins, *et al.*, "Fiber grating sensors," *Journal of lightwave technology,* vol. 15, pp. 1442-1463, 1997.

[59] V. Bhatia and A. M. Vengsarkar, "Optical fiber long-period grating sensors," *Optics Letters,* vol. 21, pp. 692-694, 1996.

[60] K. O. Hill and G. Meltz, "Fiber Bragg grating technology fundamentals and overview," *Journal of lightwave technology,* vol. 15, pp. 1263-1276, 1997.

[61] T. Imai, T. Komukai, and M. Nakazawa, "Dispersion tuning of a linearly chirped fiber Bragg grating without a center wavelength shift by applying a strain gradient," *Photonics Technology Letters, IEEE,* vol. 10, pp. 845-847, 1998.

[62] K. Feng, J.-X. Chai, V. Grubsky, D. Starodubov, M. Hayee, S. Lee, *et al.*, "Dynamic dispersion compensation in a 10-Gb/s optical system using a novel voltage tuned nonlinearly chirped fiber Bragg grating," *Photonics Technology Letters, IEEE,* vol. 11, pp. 373-375, 1999.

[63] Y. Okabe, R. Tsuji, and N. Takeda, "Application of chirped fiber Bragg grating sensors for identification of crack locations in composites," *Composites Part A: applied science and manufacturing,* vol. 35, pp. 59-65, 2004.

[64] G. Laffont and P. Ferdinand, "Tilted short-period fibre-Bragg-grating-induced coupling to cladding modes for accurate refractometry," *Measurement Science and Technology,* vol. 12, p. 765, 2001.

[65] T. Erdogan and J. Sipe, "Tilted fiber phase gratings," *JOSA A,* vol. 13, pp. 296-313, 1996.

[66] S. W. James and R. P. Tatam, "Optical fibre long-period grating sensors: characteristics and application," *Measurement Science and Technology,* vol. 14, pp. R49-R61, 2003.

[67] Z. Wang, J. Heflin, K. Van Cott, R. H. Stolen, S. Ramachandran, and S. Ghalmi, "Biosensors employing ionic self-assembled multilayers adsorbed on long-period fiber gratings," *Sensors and Actuators B: Chemical,* vol. 139, pp. 618-623, 2009.

[68] J. Homola, S. S. Yee, and G. Gauglitz, "Surface plasmon resonance sensors: review," *Sensors and Actuators B: Chemical,* vol. 54, pp. 3-15, 1999.

[69] J. Homola, "Surface plasmon resonance sensors for detection of chemical and biological species," *Chemical reviews,* vol. 108, pp. 462-493, 2008.

[70] W. L. Barnes, A. Dereux, and T. W. Ebbesen, "Surface plasmon subwavelength optics," *Nature*, vol. 424, pp. 824-830, 2003.

[71] C. T. Campbell and G. Kim, "SPR microscopy and its applications to high-throughput analyses of biomolecular binding events and their kinetics," *Biomaterials*, vol. 28, pp. 2380-2392, 2007.

[72] R. Slavík, J. Homola, J. Čtyroký, and E. Brynda, "Novel spectral fiber optic sensor based on surface plasmon resonance," *Sensors and Actuators B: Chemical*, vol. 74, pp. 106-111, 2001.

[73] J. H. Luong, K. B. Male, and J. D. Glennon, "Biosensor technology: technology push versus market pull," *Biotechnology advances*, vol. 26, pp. 492-500, 2008.

[74] M.-H. Chiu, S.-F. Wang, and R.-S. Chang, "D-type fiber biosensor based on surface-plasmon resonance technology and heterodyne interferometry," *Optics letters*, vol. 30, pp. 233-235, 2005.

[75] B. Lee, "Review of the present status of optical fiber sensors," *Optical Fiber Technology*, vol. 9, pp. 57-79, 2003.

[76] E. Krioukov, D. Klunder, A. Driessen, J. Greve, and C. Otto, "Sensor based on an integrated optical microcavity," *Optics letters*, vol. 27, pp. 512-514, 2002.

[77] A. Yalcin, K. C. Popat, J. C. Aldridge, T. A. Desai, J. Hryniewicz, N. Chbouki, *et al.*, "Optical sensing of biomolecules using microring resonators," *Selected Topics in Quantum Electronics, IEEE Journal of*, vol. 12, pp. 148-155, 2006.

[78] J. Ward and O. Benson, "WGM microresonators: sensing, lasing and fundamental optics with microspheres," *Laser & Photonics Reviews*, vol. 5, pp. 553-570, 2011.

[79] V. S. Ilchenko and A. B. Matsko, "Optical resonators with whispering-gallery modes-part II: applications," *Selected Topics in Quantum Electronics, IEEE Journal of*, vol. 12, pp. 15-32, 2006.

[80] H. C. Tapalian and J.-P. Laine, "Optical microcavity resonator sensor," ed: Google Patents, 2003.

[81] H. C. Tapalian and J.-P. Laine, "Coated optical microcavity resonator chemical sensor," ed: Google Patents, 2003.

[82] S. Arnold, M. Khoshsima, I. Teraoka, S. Holler, and F. Vollmer, "Shift of whispering-gallery modes in microspheres by protein adsorption," *Optics Letters*, vol. 28, pp. 272-274, 2003.

[83] N. M. Hanumegowda, C. J. Stica, B. C. Patel, I. White, and X. Fan, "Refractometric sensors based on microsphere resonators," *Applied Physics Letters,* vol. 87, p. 201107, 2005.

[84] F. Xu, P. Horak, and G. Brambilla, "Optical microfiber coil resonator refractometric sensor," *Optics Express,* vol. 15, pp. 7888-7893, 2007.

[85] F. Xu, V. Pruneri, V. Finazzi, and G. Brambilla, "An embedded optical nanowire loop resonator refractometric sensor," *Optics Express,* vol. 16, pp. 1062-1067, 2008.

[86] C.-Y. Chao, W. Fung, and L. J. Guo, "Polymer microring resonators for biochemical sensing applications," *Selected Topics in Quantum Electronics, IEEE Journal of,* vol. 12, pp. 134-142, 2006.

[87] C.-Y. Chao and L. J. Guo, "Design and optimization of microring resonators in biochemical sensing applications," *Journal of Lightwave Technology,* vol. 24, p. 1395, 2006.

[88] J.-R. Carrier, M. Boissinot, and C. N. Allen, "Dielectric resonating microspheres for biosensing: An optical approach to a biological problem," *American Journal of Physics,* vol. 82, pp. 510-520, 2014.

[89] X. Fan and I. M. White, "Optofluidic microsystems for chemical and biological analysis," *Nature photonics,* vol. 5, pp. 591-597, 2011.

[90] F. Vollmer, D. Braun, A. Libchaber, M. Khoshsima, I. Teraoka, and S. Arnold, "Protein detection by optical shift of a resonant microcavity," *Applied Physics Letters,* vol. 80, pp. 4057-4059, 2002.

[91] S. Blair and Y. Chen, "Resonant-enhanced evanescent-wave fluorescence biosensing with cylindrical optical cavities," *Applied Optics,* vol. 40, pp. 570-582, 2001.

[92] D. Armani, B. Min, A. Martin, and K. J. Vahala, "Electrical thermo-optic tuning of ultrahigh-Q microtoroid resonators," *Applied physics letters,* vol. 85, pp. 5439-5441, 2004.

[93] A. Francois and M. Himmelhaus, "Optical biosensor based on whispering gallery mode excitations in clusters of microparticles," *Applied Physics Letters,* vol. 92, p. 141107, 2008.

[94] M. Rosenblit, P. Horak, S. Helsby, and R. Folman, "Single-atom detection using whispering-gallery modes of microdisk resonators," *Physical Review A,* vol. 70, p. 053808, 2004.

[95] L. He, Y.-F. Xiao, C. Dong, J. Zhu, V. Gaddam, and L. Yang, "Compensation of thermal refraction effect in high-Q toroidal microresonator by polydimethylsiloxane coating," *Applied Physics Letters,* vol. 93, p. 201102, 2008.

[96] J. S. Seo, D. Whang, H. Lee, S. Im Jun, J. Oh, Y. J. Jeon, *et al.*, "A homochiral metal–organic porous material for enantioselective separation and catalysis," *Nature,* vol. 404, pp. 982-986, 2000.

[97] D. N. Dybtsev, H. Chun, S. H. Yoon, D. Kim, and K. Kim, "Microporous manganese formate: a simple metal-organic porous material with high framework stability and highly selective gas sorption properties," *Journal of the American Chemical Society,* vol. 126, pp. 32-33, 2004.

[98] N. Lin, L. Jiang, S. Wang, L. Yuan, H. Xiao, Y. Lu, *et al.*, "Ultrasensitive chemical sensors based on whispering gallery modes in a microsphere coated with zeolite," *Applied optics,* vol. 49, pp. 6463-6471, 2010.

[99] S. Li, L. Nguyen, H. Xiong, M. Wang, T. C.-C. Hu, J.-X. She, *et al.*, "Porous-wall hollow glass microspheres as novel potential nanocarriers for biomedical applications," *Nanomedicine: Nanotechnology, Biology and Medicine,* vol. 6, pp. 127-136, 2010.

[100] H. Wang, L. Yuan, C. W. Kim, Q. Han, T. Wei, X. Lan, *et al.*, "Optical microresonator based on hollow sphere with porous wall for chemical sensing," *Optics Letters,* vol. 37, pp. 94-96, 2012.

[101] I. Teraoka and S. Arnold, "Enhancing the sensitivity of a whispering-gallery mode microsphere sensor by a high-refractive-index surface layer," *JOSA B,* vol. 23, pp. 1434-1441, 2006.

[102] I. Teraoka and S. Arnold, "Theory of resonance shifts in TE and TM whispering gallery modes by nonradial perturbations for sensing applications," *JOSA B,* vol. 23, pp. 1381-1389, 2006.

[103] I. Teraoka, S. Arnold, and F. Vollmer, "Perturbation approach to resonance shifts of whispering-gallery modes in a dielectric microsphere as a probe of a surrounding medium," *JOSA B,* vol. 20, pp. 1937-1946, 2003.

[104] H. Wang, L. Yuan, J. Huang, X. Lan, C.-W. Kim, L. Jiang, *et al.*, "Computational Modeling and Experimental Study on Optical Microresonators Using Optimal Spherical Structure for Chemical Sensing," *Advanced Chemical Engineering Research,* vol. 2, 2013.

[105] H. Wang, L. Yuan, C.-W. Kim, Q. Han, T. Wei, X. Lan, *et al.*, "Optical microresonator based on hollow sphere with porous wall for chemical sensing," *Optics letters,* vol. 37, pp. 94-96, 2012.

[106] M. L. Gorodetsky and V. S. Ilchenko, "Optical microsphere resonators: optimal coupling to high-< i> Q</i> whispering-gallery modes," *JOSA B,* vol. 16, pp. 147-154, 1999.

[107] B. Little, J.-P. Laine, D. Lim, H. Haus, L. Kimerling, and S. Chu, "Pedestal antiresonant reflecting waveguides for robust coupling to microsphere resonators and for microphotonic circuits," *Optics Letters,* vol. 25, pp. 73-75, 2000.

[108] A. Serpengüzel, G. Griffel, and S. Arnold, "Excitation of resonances of microspheres on an optical fiber," *Optics Letters,* vol. 20, pp. 654-656, 1995.

[109] N. Dubreuil, J. Knight, D. Leventhal, V. Sandoghdar, J. Hare, and V. Lefevre, "Eroded monomode optical fiber for whispering-gallery mode excitation in fused-silica microspheres," *Optics letters,* vol. 20, pp. 813-815, 1995.

[110] V. S. Ilchenko, X. S. Yao, and L. Maleki, "Pigtailing the high-< i> Q</i> microsphere cavity: a simple fiber coupler for optical whispering-gallery modes," *Optics letters,* vol. 24, pp. 723-725, 1999.

[111] H. Wang, X. Lan, J. Huang, L. Yuan, C.-W. Kim, and H. Xiao, "Fiber pigtailed thin wall capillary coupler for excitation of microsphere WGM resonator," *Optics express,* vol. 21, pp. 15834-15839, 2013.

[112] C. Bray, *Dictionary of glass: materials and techniques*: University of Pennsylvania Press, 2001.

[113] M. Cai, O. Painter, and K. J. Vahala, "Observation of Critical Coupling in a Fiber Taper to a Silica-Microsphere Whispering-Gallery Mode System," *Physical Review Letters,* vol. 85, pp. 74-77, 07/03/ 2000.

[114] L. Yuan, T. Wei, Q. Han, H. Wang, J. Huang, L. Jiang, *et al.*, "Fiber inline Michelson interferometer fabricated by a femtosecond laser," *Optics Letters,* vol. 37, pp. 4489-4491, 2012/11/01 2012.

[115] S. Kellomäki, K.-Y. Wang, and M. Lemettinen, "Controlled environment chambers for investigating tree response to elevated CO2 and temperature under boreal conditions," *Photosynthetica,* vol. 38, pp. 69-81, 2000.

[116] R. Vadivambal and D. Jayas, "Non-uniform temperature distribution during microwave heating of food materials—A review," *Food and Bioprocess Technology,* vol. 3, pp. 161-171, 2010.

[117] D. Ross, M. Gaitan, and L. E. Locascio, "Temperature measurement in microfluidic systems using a temperature-dependent fluorescent dye," *Analytical chemistry*, vol. 73, pp. 4117-4123, 2001.

[118] Y.-J. Rao, "In-fibre Bragg grating sensors," *Measurement science and technology*, vol. 8, p. 355, 1997.

[119] J. Mandal, S. Pal, T. Sun, K. T. Grattan, A. T. Augousti, and S. A. Wade, "Bragg grating-based fiber-optic laser probe for temperature sensing," *Photonics Technology Letters, IEEE*, vol. 16, pp. 218-220, 2004.

[120] T. Wei, X. Lan, and H. Xiao, "Fiber Inline Core–Cladding-Mode Mach–Zehnder Interferometer Fabricated by Two-Point CO Laser Irradiations," *Photonics Technology Letters, IEEE*, vol. 21, pp. 669-671, 2009.

[121] C. H. Dong, L. He, Y. F. Xiao, V. R. Gaddam, S. K. Ozdemir, Z. F. Han, *et al.*, "Fabrication of high- Q polydimethylsiloxane optical microspheres for thermal sensing," *Applied Physics Letters*, vol. 94, 2009.

[122] B. B. Li, Q. Y. Wang, Y. F. Xiao, X. F. Jiang, Y. Li, L. Xiao, *et al.*, "On chip, high-sensitivity thermal sensor based on high- Q polydimethylsiloxane-coated microresonator," *Applied Physics Letters*, vol. 96, 2010.

[123] V. Bhatia, "Applications of long-period gratings to single and multi-parameter sensing," *Optics Express*, vol. 4, pp. 457-466, 1999.

[124] E.-S. Kang, T.-H. Lee, and B.-S. Bae, "Measurement of the thermo-optic coefficients in sol-gel derived inorganic–organic hybrid material films," *Applied physics letters*, vol. 81, pp. 1438-1440, 2002.

[125] I. M. White, H. Oveys, and X. Fan, "Liquid-core optical ring-resonator sensors," *Optics Letters*, vol. 31, pp. 1319-1321, 2006.

[126] H. Zhu, I. M. White, J. D. Suter, P. S. Dale, and X. Fan, "Analysis of biomolecule detection with optofluidic ring resonator sensors," *Optics Express*, vol. 15, pp. 9139-9146, 2007.

[127] I. M. White, H. Zhu, J. D. Suter, N. M. Hanumegowda, H. Oveys, M. Zourob, *et al.*, "Refractometric sensors for lab-on-a-chip based on optical ring resonators," *Sensors Journal, IEEE*, vol. 7, pp. 28-35, 2007.

[128] R. P. Swatloski, S. K. Spear, J. D. Holbrey, and R. D. Rogers, "Dissolution of cellose with ionic liquids," *Journal of the American Chemical Society*, vol. 124, pp. 4974-4975, 2002.

[129] J. Rao, K. Venkatesan, K. Nagarajan, T. Srinivasan, and P. Vasudeva Rao, "Electrodeposition of metallic uranium at near ambient conditions from room temperature ionic liquid," *Journal of Nuclear Materials*, vol. 408, pp. 25-29, 2011.

[130] C. Wang, Y. Guo, X. Zhu, G. Cui, H. Li, and S. Dai, "Highly efficient CO 2 capture by tunable alkanolamine-based ionic liquids with multidentate cation coordination," *Chemical Communications*, vol. 48, pp. 6526-6528, 2012.

[131] E. D. Bates, R. D. Mayton, I. Ntai, and J. H. Davis, "CO2 capture by a task-specific ionic liquid," *Journal of the American Chemical Society*, vol. 124, pp. 926-927, 2002.

[132] J. Tang, W. Sun, H. Tang, M. Radosz, and Y. Shen, "Enhanced CO2 absorption of poly (ionic liquid) s," *Macromolecules*, vol. 38, pp. 2037-2039, 2005.